Bias Correction of the Ratio of Total Column CH4 to CO2 Retrieved from GOSAT Spectra

Haruki Oshio, Yukio Yoshida, Tsuneo Matsunaga, Nicholas Deutscher, Manvendra Dubey, David Griffith, Frank Hase, Laura Iraci, Rigel Kivi, Cheng Liu, et al.

▶ **To cite this version:**

Haruki Oshio, Yukio Yoshida, Tsuneo Matsunaga, Nicholas Deutscher, Manvendra Dubey, et al.. Bias Correction of the Ratio of Total Column CH4 to CO2 Retrieved from GOSAT Spectra. Remote Sensing, 2020, 12 (19), pp.3155. 10.3390/rs12193155 . hal-03958622

HAL Id: hal-03958622

https://cnrs.hal.science/hal-03958622

Submitted on 27 Jan 2023

HAL is a multi-disciplinary open access archive for the deposit and dissemination of scientific research documents, whether they are published or not. The documents may come from teaching and research institutions in France or abroad, or from public or private research centers.

L'archive ouverte pluridisciplinaire **HAL**, est destinée au dépôt et à la diffusion de documents scientifiques de niveau recherche, publiés ou non, émanant des établissements d'enseignement et de recherche français ou étrangers, des laboratoires publics ou privés.

Distributed under a Creative Commons Attribution 4.0 International License

remote sensing

MDPI

Article

Bias Correction of the Ratio of Total Column CH_4 to CO_2 Retrieved from GOSAT Spectra

Haruki Oshio [1,*], Yukio Yoshida [1], Tsuneo Matsunaga [1], Nicholas M. Deutscher [2], Manvendra Dubey [3], David W. T. Griffith [2], Frank Hase [4], Laura T. Iraci [5], Rigel Kivi [6], Cheng Liu [7,8], Isamu Morino [1], Justus Notholt [9], Young-Suk Oh [10], Hirofumi Ohyama [1], Christof Petri [9], David F. Pollard [11], Coleen Roehl [12], Kei Shiomi [13], Ralf Sussmann [14], Yao Té [15], Voltaire A. Velazco [2], Thorsten Warneke [9] and Debra Wunch [16]

1 Center for Global Environmental Research, National Institute for Environmental Studies, Tsukuba, Ibaraki 305-8506, Japan; yoshida.yukio@nies.go.jp (Y.Y.); matsunag@nies.go.jp (T.M.); morino@nies.go.jp (I.M.); oyama.hirofumi@nies.go.jp (H.O.)
2 Centre for Atmospheric Chemistry, School of Earth, Atmospheric and Life Sciences, Faculty of Science, Medicine and Health, University of Wollongong, Wollongong 2522, Australia; ndeutsch@uow.edu.au (N.M.D.); griffith@uow.edu.au (D.W.T.G.); voltaire@uow.edu.au (V.A.V.)
3 Los Alamos National Laboratory, Los Alamos, NM 87545, USA; dubey@lanl.gov
4 Institute of Meteorology and Climate Research IMK-ASF, Karlsruhe Institute of Technology, 76021 Karlsruhe, Germany; frank.hase@kit.edu
5 Atmospheric Science Branch, NASA Ames Research Center, Moffett Field, CA 94035, USA; laura.t.iraci@nasa.gov
6 Space and Earth Observation Centre, Finnish Meteorological Institute, 99600 Sodankylä, Finland; rigel.kivi@fmi.fi
7 Key Laboratory of Environmental Optics and Technology, Anhui Institute of Optics and Fine Mechanics, Chinese Academy of Sciences, Hefei 230031, China; Chliu81@ustc.edu.cn
8 Department of Precision Machinery and Precision Instrumentation, University of Science and Technology of China, Hefei 230026, China
9 Institute of Environmental Physics, University of Bremen, 28359 Bremen, Germany; jnotholt@iup.physik.uni-bremen.de (J.N.); christof_p@iup.physik.uni-bremen.de (C.P.); warneke@iup.physik.uni-bremen.de (T.W.)
10 Climate Research Division, National Institute of Meteorological Sciences, Seogwipo, Jeju-do 63568, Korea; ysoh306@korea.kr
11 National Institute of Water and Atmospheric Research, Lauder, Omakau 9352, New Zealand; dave.pollard@niwa.co.nz
12 Division of Geology and Planetary Science, California Institute of Technology, Pasadena, CA 91125, USA; coleen@caltech.edu
13 Japan Aerospace Exploration Agency (JAXA), Tsukuba, Ibaraki 305-8505, Japan; shiomi.kei@jaxa.jp
14 Institute of Meteorology and Climate Research—Atmospheric Environmental Research (IMK-IFU), Karlsruhe Institute of Technology, 82467 Garmisch-Partenkirchen, Germany; ralf.sussmann@kit.edu
15 Laboratoire d'Etudes du Rayonnement et de la Matière en Astrophysique et Atmosphères (LERMA-IPSL), Sorbonne Université, CNRS, Observatoire de Paris, PSL Université, 75005 Paris, France; yao-veng.te@upmc.fr
16 Department of Physics, University of Toronto, Toronto, ON M5S 1A7, Canada; dwunch@atmosp.physics.utoronto.ca
* Correspondence: oshio.haruki@nies.go.jp; Tel.: +81-29-850-2416

Received: 21 August 2020; Accepted: 24 September 2020; Published: 25 September 2020

Abstract: The proxy method, using the ratio of total column CH_4 to CO_2 to reduce the effects of common biases, has been used to retrieve column-averaged dry-air mole fraction of CH_4 from satellite data. The present study characterizes the remaining scattering effects in the CH_4/CO_2 ratio component of the Greenhouse gases Observing SATellite (GOSAT) retrieval and uses them for bias correction. The variation of bias between the GOSAT and Total Carbon Column Observing Network (TCCON)

ratio component with GOSAT data-derived variables was investigated. Then, it was revealed that the variability of the bias could be reduced by using four variables for the bias correction—namely, airmass, 2 μm band radiance normalized with its noise level, the ratio between the partial column-averaged dry-air mole fraction of CH_4 for the lower atmosphere and that for the upper atmosphere, and the difference in surface albedo between the CH_4 and CO_2 bands. The ratio of partial column CH_4 reduced the dependence of bias on the cloud fraction and the difference between hemispheres. In addition to the reduction of bias (from 0.43% to 0%), the precision (standard deviation of the difference between GOSAT and TCCON) was reduced from 0.61% to 0.55% by the correction. The bias and its temporal variation were reduced for each site: the mean and standard deviation of the mean bias for individual seasons were within 0.2% for most of the sites.

Keywords: methane; proxy method; GOSAT; TCCON

1. Introduction

Atmospheric methane (CH_4) is the most significant anthropogenic greenhouse gas after carbon dioxide (CO_2) and is emitted from both anthropogenic and natural sources. Satellite observation, which can obtain data over wide areas, is effective to elucidate the CH_4 budget over the globe. In the last 15 years, the column-averaged dry-air mole fraction of methane (XCH_4) has been retrieved from the spectra of the backscattered Short-Wavelength InfraRed (SWIR) sunlight measured by sensors onboard satellites [1–6]. Satellite-derived XCH_4 data have been applied to the inverse modeling of CH_4 sources and sinks [7–11]. High precision and small bias in spatiotemporal variation are required for the XCH_4 data to be used in inverse modeling [12,13]. It is possible that even a small regional bias (0.5%) in the XCH_4 data can lead to significant errors in regional source and sink estimation [12]. Optical path length modification due to the light scatterings by aerosols and clouds is a large source of error for the satellite-based SWIR retrievals [14–16]. The degree of optical path length modification depends on the abundance, optical properties, and vertical distributions of aerosols and clouds and the reflectance of ground surfaces.

Two retrieval methods have been used to reduce systematic biases due to atmospheric scatterings: the full-physics method and the proxy method. In the full-physics method, the existence of aerosols is described in the forward model, and the aerosol-related parameters are simultaneously retrieved with the gas abundance [17,18]. In the proxy method, information on the optical path length modification for the CH_4 absorption band is obtained from that for the adjacent CO_2 absorption band [2] (Equation (1)),

$$XCH_4 = \frac{XCH_{4,clr}}{XCO_{2,clr}} \times XCO_{2,mdl}, \quad (1)$$

where $XCH_{4,clr}$ and $XCO_{2,clr}$ are XCH_4 and XCO_2 retrieved under a clear-sky assumption (no aerosols and clouds are assumed) and $XCO_{2,mdl}$ is XCO_2 from the numerical model. It is assumed that, in the ratio component ($XCH_{4,clr}/XCO_{2,clr}$), the impacts of aerosol and clouds cancel each other out between $XCH_{4,clr}$ and $XCO_{2,clr}$. It is also assumed that the relative variation of XCO_2 is much smaller than that of XCH_4, and that XCO_2 is well represented by the numerical model. The proxy method is expected to offer a larger amount of useful retrieved data than the full-physics method, since highly cloud- and aerosol-loaded scenes are difficult to handle in the current full-physics algorithms [19–22].

Both errors in the ratio component and the model XCO_2 lead to errors in the resulting XCH_4. Butz et al. [23] showed that the scattering-related errors are not perfectly canceled out in the ratio component depending on atmospheric and ground surface conditions (i.e., cirrus and aerosol load and surface albedo). Schepers et al. [19] discussed the possibility that the temporal variation of bias in proxy XCH_4 corresponds to that of bias in the ratio component. In the case of inverse modeling, Parker et al. [24] suggested that it is beneficial to use the ratio component with each own XCO_2

model that is consistent with the XCH_4 model used in the inversion. The ratio component can also be directly inverted [25–27]. The ratio component derived from the Greenhouse gases Observing SATellite (GOSAT) data has been validated by comparing it with that derived from the Total Carbon Column Observing Network (TCCON) data [19,24,26,28,29]. However, it has not been fully investigated what range of cloud and aerosol load permits the canceling out of scattering-related errors in the ratio component. In general, the criteria for the cloud and aerosol screening have been chosen by the algorithm developer. Scattering-related errors are expected to remain and to cause bias in the resulting XCH_4, especially when relaxing the data-screening criteria, although this increases the data throughput. Bias corrections of the proxy-based XCH_4 have been conducted; however, a simple linear relationship between the bias and the surface albedo [30] and a simple global bias correction [29,31] have been used.

The present study sought to characterize the bias in the GOSAT ratio component and develop a method for correcting the bias while considering the atmospheric scattering effects. GOSAT has been operating for more than 10 years, allowing us to investigate the variation of the bias with time and space and its factors. The ratio component derived from TCCON data was used as the ground truth. In Section 2, the data used and its processing are described. In Section 3, the relationship between the bias and the related variables derived from GOSAT data is investigated. In Section 4, the bias correction is conducted based on the results of Section 3, and the corrected results are evaluated.

2. Materials and Data Processing

2.1. GOSAT Data

GOSAT was launched on 23 January 2009 and is on a sun-synchronous orbit at 666 km altitude with 3-day recurrence and a descending node around 13:00 local time. It is equipped with two instruments: the Thermal And Near-infrared Sensor for carbon Observation–Fourier Transform Spectrometer (TANSO-FTS) and the Cloud and Aerosol Imager (TANSO-CAI). The TANSO-FTS has three bands in the Short-Wavelength InfraRed (SWIR) region (an O_2 A band, a weak CO_2 absorption band, and a strong CO_2 absorption band (Bands 1, 2, and 3) centered at 0.76, 1.6, and 2.0 μm, respectively) and records two orthogonal polarization components (hereafter called P/S components). For the signal processing of the TANSO-FTS, the amplifier gain level can be controlled at different levels, high (H) and medium (M), according to the brightness of the target. Gain M is used over bright surfaces such as the Sahara and central Australia. The instantaneous field of view (IFOV) of the TANSO-FTS is 15.8 mrad, which corresponds to a circular surface footprint of about 10.5 km in diameter at nadir. The TANSO-FTS L1B product (radiance spectral data) version V210.210 was used in the present study. We used spectra acquired from April 2009 to December 2018. The sensitivity degradation of the TANSO-FTS was corrected using a radiometric degradation model that is based on the on-orbit solar calibration data [32]. The P and S polarization components of the observed spectra were synthesized to produce a total intensity spectrum [5]. The TANSO-CAI is a push-broom imager and has four narrow bands in the near-ultraviolet to near-infrared regions centered at 0.38, 0.674, 0.87, and 1.6 μm with spatial resolutions of 0.5, 0.5, 0.5, and 1.5 km, respectively, for nadir pixels. The TANSO-CAI L2 cloud flag product (integrated clear confidence level for each TANSO-CAI pixel) version V02.00 was used in the present study. The integrated clear confidence level expresses the cloudy area with 0, the clear area with 1, and the ambiguous area with a numerical value between 0 and 1 [33].

2.2. Retrieval

The spectral windows of 1.626–1.695 μm and 1.567–1.618 μm within the TANSO-FTS Band 2 were used to retrieve $XCH_{4,clr}$ and $XCO_{2,clr}$ under the clear-sky assumption, respectively, using the same retrieval scheme as in the NIES TANSO-FTS L2 SWIR full-physics retrieval [5,21,34]. The atmospheric column was divided into 15 layers from the surface to 0.1 hPa with a constant pressure difference, and the average gas concentration for each layer was retrieved. As an indicator of optical path length modification, the surface pressure (P_{srf}) under the clear-sky assumption was also retrieved from the

TANSO-FTS Band 1 spectra. The state vector for the retrieval of each band also included the surface albedo and the wavenumber dispersion. The surface albedo was retrieved at several wavenumber grid points within each band (CH_4, CO_2, and O_2 A) [5]. The mean value was calculated for each band and was used in the following analysis. Data satisfying all the following criteria were used for the subsequent analysis: (1) several data-quality flags stored in the TANSO-FTS L1B product and spectrum quality check utilizing the out-of-band spectra [34] are set as OK; (2) the solar zenith angle is <70°; (3) the land fraction of the TANSO-FTS footprint is ≥60%; (4) the mean squared value of the residual spectrum of the CO_2 band is≤ 4; and (5) the degree of freedom for signals (DFS) is ≥1 for both $XCH_{4,clr}$ and $XCO_{2,clr}$.

2.3. Variables for Explaining the Bias in the Ratio Component

Butz et al. [23] evaluated the accuracy of the ratio component and analyzed the error sources (the reasons why the scattering-related errors were not canceled in the ratio component) using simulated satellite measurements. They used cloud-free aerosol-loaded and cirrus-loaded scenes that were assumed to be the targets of the full-physics method. They showed that the primary sources of error were the difference in surface albedo between the CH_4 band and the CO_2 band and the difference in the retrieval sensitivity to scattering effects at each height level between these bands. The impact of these sources is expected to vary according to the amount and vertical distribution of the scattering materials.

In the studies validating the ratio component derived from the actual GOSAT data [19,24,26,28], the cloud screening was conducted using the cloud fraction within the IFOV of the TANSO-FTS provided by the TANSO-CAI onboard GOSAT. The TANSO-CAI is prone to fail to detect optically thin cirrus clouds [35]. In several studies (e.g., [19]), cirrus-loaded scenes were screened out using the information from the TANSO-FTS 2 μm band. More specifically, if the TANSO-FTS signal level at the strong water vapor absorption channels exceeds the noise level, elevated scattering materials (mainly cirrus cloud) are expected [5,36]. However, it has not been fully addressed how well the cloud fraction and the 2 μm band signal are related to the bias in the ratio component (i.e., the systematic difference between GOSAT and TCCON). Therefore, we investigated the variation of the bias with the cloud fraction and the 2 μm band signal. The cloud fraction (f_c) was defined as the ratio of TANSO-CAI pixels with an integrated clear confidence level lower than 0.33 and all TANSO-CAI pixels within the TANSO-FTS IFOV in this study. The TANSO-CAI tends to identify the pixels over snow and ice surfaces as cloudy pixels. Thus, we calculated the Normalized Difference Snow Index ($NDSI = (\rho_{O2} - \rho_{CH4})/(\rho_{O2} + \rho_{CH4})$, where ρ_{O2} and ρ_{CH4} are the retrieved surface albedo for the O_2 A band and the CH_4 band, respectively), and used data having NDSI ≤ 0.4 for investigating the relationship between the bias and f_c. The threshold value of 0.4 was empirically determined (Figure S1). The radiance at the strong water vapor absorptive channels normalized with its noise level in the TANSO-FTS Band 3 ($I_{2\mu m}$) was calculated in a manner similar to [5,34].

In the bias correction of the proxy method, possible error sources (e.g., those indicated by Butz et al. [23]) have hardly been considered. The correction has been conducted based on the relationship between the bias and the retrieved surface albedo [30] and by a simple global bias correction [29,31]. The bias in the ratio component has also been corrected using the surface albedo [26]. Then, we investigated the relationship between the bias in the ratio component and the related variables while considering f_c and $I_{2\mu m}$. For the related variables, the difference in the surface albedo between the CH_4 and CO_2 bands, the surface albedo, the vertical profile of CH_4 and CO_2, the airmass, and the deviation of the clear-sky surface pressure from its prior value were considered. The details of the variables are described below.

The differences in surface albedo and the vertical profile have been revealed as important error sources [23]. For the difference in surface albedo, the retrieved albedo values (ρ_{CH4} and ρ_{CO2}) were used ($\Delta_{alb} = \rho_{CH4} - \rho_{CO2}$). Albedo itself ($\rho_{CH4}$) was also used, since it has been used to explain the bias of the proxy method [26,30] and the full-physics method [37]. For the vertical profile, the partial column-averaged dry-air mole fractions were calculated for Layers 1–7 (upper atmosphere,

0–0.47P_{srf} hPa ($XCH_{4,upper}$ and $XCO_{2,upper}$)) and for Layers 12–15 (lower atmosphere, 0.73P_{srf}–P_{srf} hPa ($XCH_{4,lower}$ and $XCO_{2,lower}$)). See Section 2.2 for the definition of layers. The range of the calculation (1–7 layers and 12–15 layers) was decided by considering the averaging kernel (Figure S2). It is well-known that the SWIR retrieval has a slight sensitivity to the detailed profile but has a known sensitivity to the lower atmosphere (e.g., [38]); therefore, the ratios (R_{CH4} = $XCH_{4,lower}/XCH_{4,upper}$ and R_{CO2} = $XCO_{2,lower}/XCO_{2,upper}$) were used to represent the characteristics of the vertical profile. Airmass is expected to be related to the impact of optical path length modification on the retrieval of $XCH_{4,clr}$ and $XCO_{2,clr}$. The approximate airmass was calculated as (1/cos(solar zenith angle) + 1/cos(observing zenith angle)), which was similar to the previous studies that conducted bias correction for the full-physics method by considering airmass [37,39]. For the full-physics method, the deviation of the retrieved surface pressure from its prior value was also used for the bias correction [37,39]. In the case of the clear-sky retrieval, the deviation simply indicates the degree of optical path length modification for the O_2 A band and has been used for the cloud screening [40]. The deviation is expected to contain information about the scattering effect by aerosols that can be hardly accounted for by f_c and $I_{2\mu m}$. Then, the deviation of the clear-sky surface pressure from its prior value was calculated as (ΔP_{srf} = $P_{srf,retrieve}$ − $P_{srf,prior}$).

2.4. TCCON Data and Matching with GOSAT Data

TCCON XCH_4 and XCO_2 data (GGG2014) from 26 sites [41–67] were used as the ground truth to validate the GOSAT ratio component. The map of the sites is shown in Figure A1, and the overview of the sites is shown in Table A1. The TCCON XCH_4 and XCO_2 data used in the present study ($XCH_{4,TCCON}$ and $XCO_{2,TCCON}$) represent the mean values measured at each TCCON site within ±30 min of the GOSAT observation time. GOSAT data were selected within a ±2° latitude/longitude box centered at each TCCON site and within the difference in altitude between GOSAT (average within footprint) and TCCON site of 400 m. The ratio component of TCCON was then calculated ($XCH_{4,TCCON}/XCO_{2,TCCON}$). The relative difference (Δ_{ratio}) was calculated to evaluate the GOSAT ratio component as

$$\Delta_{ratio} = 100 \times (X_{ratio,G} - X_{ratio,T})/X_{ratio,T}, \quad (2)$$

where $X_{ratio,G}$ and $X_{ratio,T}$ are the ratio components of GOSAT and TCCON, respectively. Most of the matched GOSAT data were acquired with gain H. Therefore, the data acquired with gain H were used in the following analysis. The data acquired with gain M are briefly addressed in the latter part of the analysis.

3. Investigating the Bias in the Ratio Component

3.1. Comparison Between GOSAT and TCCON Under Cloud-Free Conditions

First, in order to confirm the baseline of the bias, $X_{ratio,G}$ was compared with $X_{ratio,T}$ under the conditions in which cloud-free scenes were expected (f_c = 0 and $I_{2\mu m} \leq 1$). Figure 1 shows the scatterplot of the ratio component and the latitudinal variation of the bias, precision of single scan, and interseasonal bias for each TCCON site. The bias and precision are defined as the mean and standard deviation of Δ_{ratio}, respectively. This precision value was used with the number of data to calculate the standard error of the mean value. The interseasonal bias is the standard deviation of bias values of the four seasons (DJF, MAM, JJA, SON) regardless of year, which has been used to represent the seasonal variability of bias [68]. The intersite bias is the standard deviation of bias values for individual TCCON sites, which is related to the spatial variability of bias. Only sites having more than nine data points were included in the calculation of intersite bias. The intersite bias of 0.14% might indicate that the spatial variation of bias is sufficiently small; however, the influence of loosening the cloud screening criteria and the temporal variation of bias should be investigated. Previous studies validating the GOSAT ratio component using TCCON data reported that the bias,

precision, and intersite bias were about 0.2–0.6%, 0.5–0.7%, and 0.15–0.2%, respectively [19,24,26,28]. Although the retrieval scheme, the version of the TANSO-FTS L1B product, the number of TCCON sites used, the data matching criteria, the cloud screening method, and other details of the data screening differ between the present study and the previous studies, the overall results were comparable.

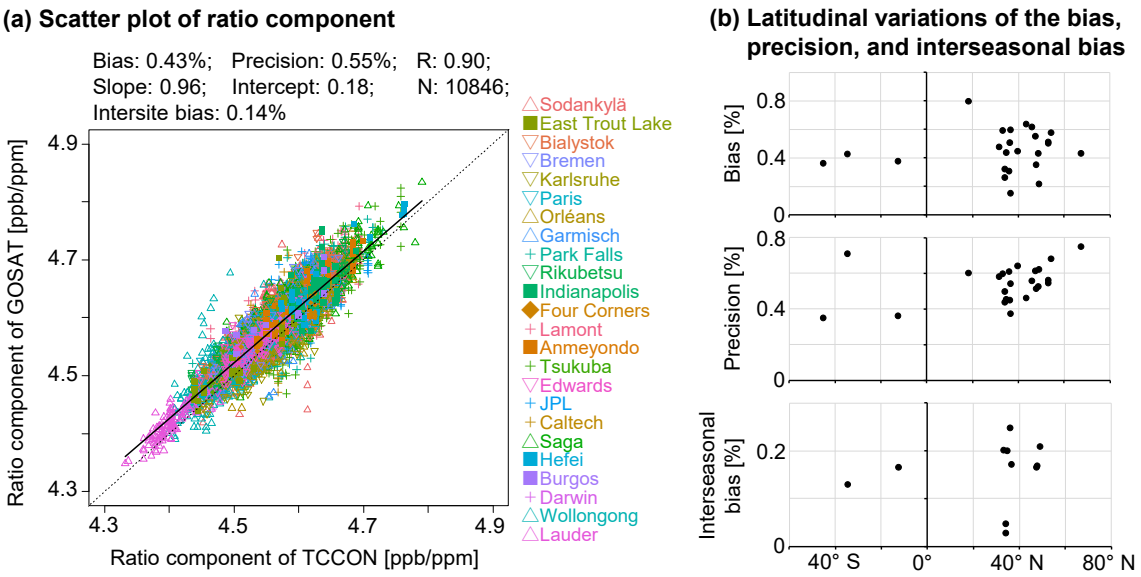

Figure 1. Comparison of the ratio component between Greenhouse gases Observing SATellite (GOSAT) and Total Carbon Column Observing Network (TCCON): (**a**) Scatter plot of individual data; (**b**) result for each site. GOSAT data obtained under conditions where cloud-free scenes were expected (cloud fraction = 0 and normalized 2 μm band radiance ≤1) were used. In (**a**), the correlation coefficient (R), the slope and intercept of the linear regression, and the number of data points (N) are also shown. In (**b**), the latitudinal variations of the bias, precision, and interseasonal bias for TCCON sites having more than nine data points are presented.

Table A2 shows that there was no clear variation of bias with tightening of the matching criteria of GOSAT and TCCON, but the precision was improved (there was a decrease in the standard deviation). Then, we assessed the influence of the matching criteria on our analysis and confirmed that the results shown below were hardly affected by the matching criteria (Appendix A). We also assessed the relationship between Δ_{ratio} and Fractional Variation in Solar Intensity (FVSI). FVSI is stored in TCCON data, and low FVSI values (≤1%) indicate a reasonably clear sky, where larger FVSI values could indicate some cirrus cloud presence. Only TCCON data having small FVSI values (≤5%) were provided to ensure the quality of XCH_4 and XCO_2 data. Figures S3 and S4 show that similar results were obtained between data with FVSI ≤ 1% and that with FVSI > 1%. This suggests that TCCON data can be used to validate the GOSAT ratio component regardless of FVSI values (0–5%).

3.2. Relationship Between Bias and Related Variables

3.2.1. Cloud Fraction and Normalized 2 μm Band Radiance

Figure 2 shows the variation of Δ_{ratio} with f_c and $I_{2\mu m}$. The data with NDSI ≤ 0.4 were used. Δ_{ratio} increases with the increase in $I_{2\mu m}$. Δ_{ratio} decreases with the increase in f_c for the data with small $I_{2\mu m}$. The large Δ_{ratio} is observed for data with both f_c and $I_{2\mu m}$ exceeding certain levels, although the amount of data is small for such cases. To interpret the information from the TANSO-CAI and the TANSO-FTS 2 μm band clearly, we mainly used the data with $f_c = 0$ and that with $I_{2\mu m} \leq 1$ in the following analysis. Most of the data fell within these cases (leftmost column and bottom row of Figure 2d). In the case of $f_c = 0$, $I_{2\mu m}$ is related to the optically thin elevated scattering materials

(mainly cirrus cloud) that were not identified by the TANSO-CAI. In the case of $I_{2\mu m} \leq 1$, f_c is related to the middle- or low-altitude clouds with a certain level of optical thickness.

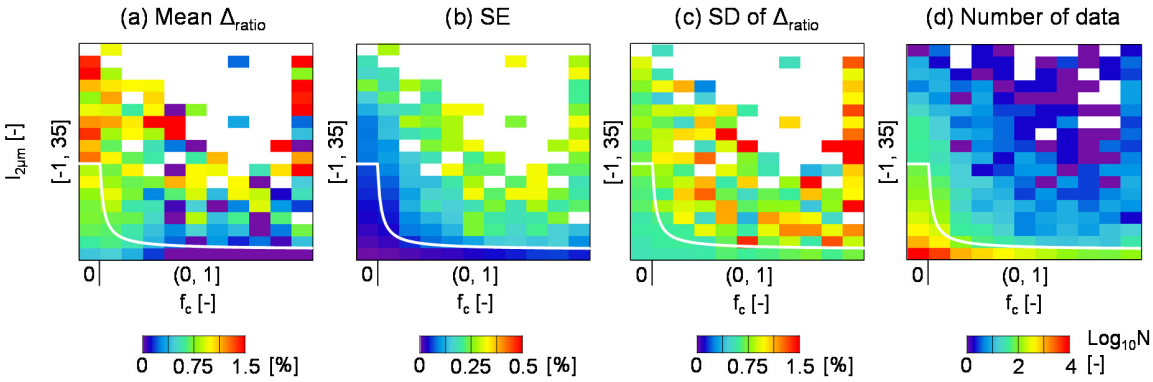

Figure 2. Variation of the relative difference in the ratio component between GOSAT and TCCON (Δ_{ratio}) according to the cloud fraction (f_c) and the normalized 2 μm band radiance ($I_{2\mu m}$). Data with $0 < f_c \leq 1$ were divided into 10 bins (horizontal axis), and data with $-1 \leq I_{2\mu m} \leq 35$ were divided into 18 bins (vertical axis). The mean Δ_{ratio}, standard error (SE) calculated by the precision of single data ((**a**,**b**)), standard deviation (SD) of Δ_{ratio} (**c**), and number of data points (**d**) for each bin are presented. Data with Normalized Difference Snow Index (NDSI) ≤ 0.4 were used. Only bins having more than two data points are colored except in panel (**d**). The white line indicates the cloud screening criterion (Section 4.3).

Figure 3a shows the variation of Δ_{ratio} with $I_{2\mu m}$. Δ_{ratio} increases with $I_{2\mu m}$. This can be attributed to the light path enhancement, which is greater for the CH_4 band than for the CO_2 band because the surface albedo of the CH_4 band is generally higher than that of the CO_2 band. The difference in vertical profile between CH_4 and CO_2 also seems to contribute to the results. More specifically, the light path enhancement means that the light repeatedly passes the area where the CH_4 concentration is higher than the column average, since the CH_4 concentration significantly decreases in the upper atmosphere. It is considered that the influence of the difference in the albedo and vertical profile becomes large with the increase in $I_{2\mu m}$.

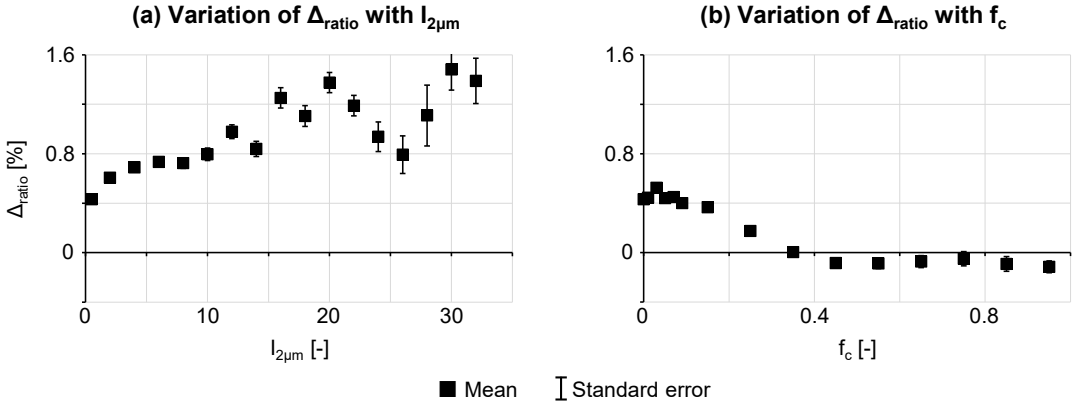

Figure 3. Variation of the relative difference in the ratio component between GOSAT and TCCON (Δ_{ratio}) according to (**a**) the normalized 2 μm band radiance ($I_{2\mu m}$) and (**b**) the cloud fraction (f_c,). Only data with $f_c = 0$ were used for (**a**), and only data with $I_{2\mu m} \leq 1$ and NDSI ≤ 0.4 were used for (**b**).

Figure 3b shows the variation of Δ_{ratio} with f_c. The data with NDSI ≤ 0.4 were used. Δ_{ratio} is 0.4% to 0.5% for the data with $f_c \leq 0.2$ and decreases with increasing f_c. This is because the effect of the difference in the retrieved surface albedo between the CH_4 and CO_2 bands becomes small with

the increase in f_c, and the influence of the upper atmosphere where the CH_4 concentration is low becomes large because of the increase in the amount of light passing through a short path (scattered at the upper part of the cloud and reaching the sensor). Although the influence of clouds depends on their height and optical thickness, it is considered that the influence of the ground surface becomes small with the increase in cloud cover. Δ_{ratio} is almost stable for the data with $f_c \geq 0.4$. It seems that the above-mentioned effects of the decreasing Δ_{ratio} and light path enhancement by clouds (multiple scattering within clouds) are balanced. Note that we obtained GOSAT data having large f_c value, which fell within the matching criteria of GOSAT and TCCON. This means that GOSAT data was obtained under cloudy conditions even when TCCON data was obtained under clear-sky conditions since cloud conditions varied within a ±2° latitude/longitude box.

3.2.2. Surface Albedo, Difference in Surface Albedo, Airmass, and Deviation of Surface Pressure

Figure 4 shows the relationship between Δ_{ratio} and the related variables (ρ_{CH4}, Δ_{alb}, airmass, and ΔP_{srf}). Section 3.2.1 showed that Δ_{ratio} was stable for data with $f_c \leq 0.2$ and increased with $I_{2\mu m}$ continuously; therefore, the results are separately plotted according to the f_c and $I_{2\mu m}$ values. Case 1: $f_c \leq 0.2$ and $I_{2\mu m} \leq 1$; Case 2: $f_c \leq 0.2$ and $I_{2\mu m} > 1$; Case 3: $f_c > 0.2$ and $I_{2\mu m} \leq 1$. The results for Case 1 are discussed in this paragraph. Δ_{ratio} increases with ρ_{CH4}, although the variation is gentler than that for the other variables (Figure 4b–d). One possible reason is that the high surface albedo is prone to bring light path enhancement, by which the influence of the difference in the vertical profile between CH_4 and CO_2 becomes large (even if the surface albedo is similar between the CH_4 and CO_2 bands). For the difference in albedo, Δ_{ratio} clearly increases with the increase in Δ_{alb}. As Butz et al. [23] indicated in their theoretical study and as discussed in the former section, the difference in albedo causes a difference in optical path length modification between the CH_4 and CO_2 bands, significantly affecting the ratio component. Δ_{ratio} decreases with an increase in airmass. The influence of optical path length modification seems to be relatively small for the cases with large airmass (the modified light path is relatively short when the geometric path is long). The characteristics of the retrieval (e.g., errors in spectroscopy) might also affect the airmass dependence. The airmass dependence of retrieved XCH_4 and XCO_2 has been corrected empirically for satellite data [37,39] and TCCON data [69,70]. Recently, Mendonca et al. [71] found that using speed-dependent Voigt line shapes for retrieval of the O_2 total column reduces the airmass dependence of TCCON XCO_2. Δ_{ratio} significantly increases with ΔP_{srf}, although the number of data with large ΔP_{srf} is small. Although ΔP_{srf} is related to the optical path length modification for the O_2 A band (TANSO-FTS Band 1), the large ΔP_{srf} indicates the possibility that the light path enhancement effect, rather than light path shortening, is dominant for Band 2. More specifically, multiple scattering might occur within the area where the concentration of CH_4 is relatively high compared to the column average. In contrast to the cases with high f_c, the fraction of light passing a short path is expected to be low, and the influence of the ground surface is expected to be large, yielding a positive bias in the ratio component.

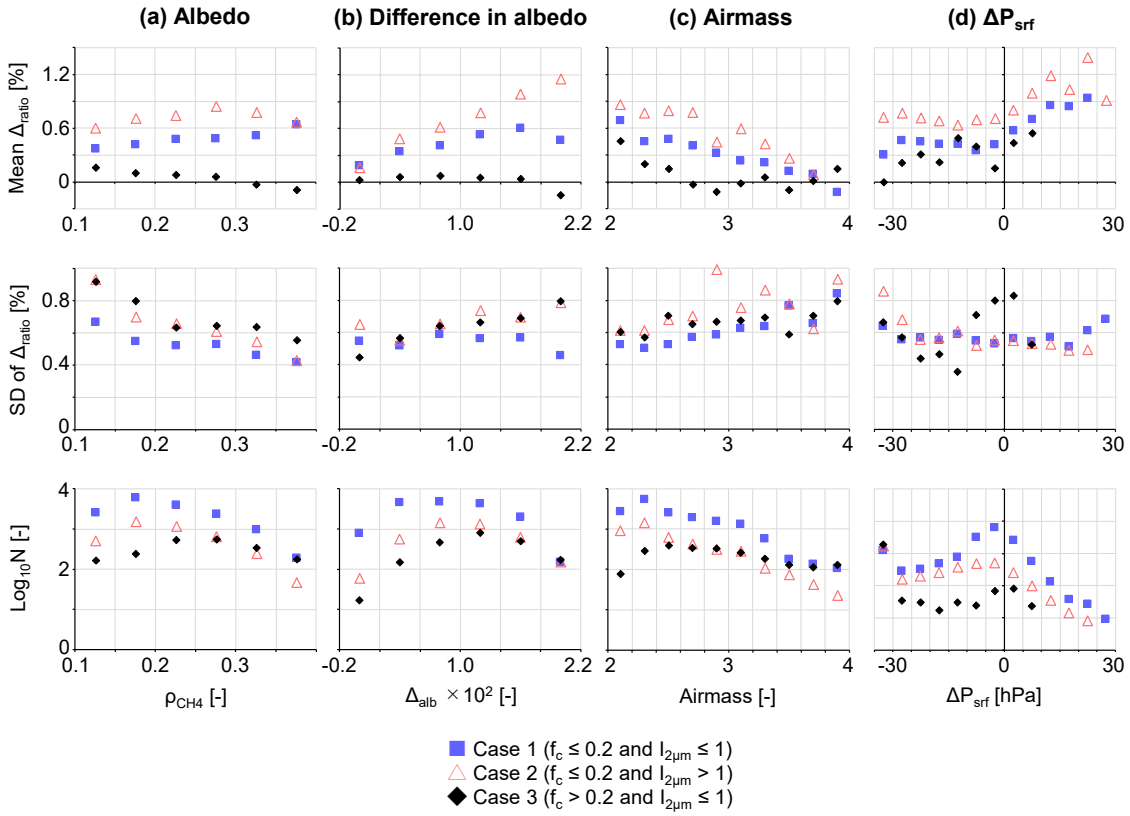

Figure 4. Variation of the relative difference in the ratio component between GOSAT and TCCON (Δ_{ratio}) according to the related variables: (**a**) retrieved surface albedo of the CH_4 band (ρ_{CH4}); (**b**) difference in the retrieved surface albedo (CH_4 band minus CO_2 band, Δ_{alb}); (**c**) airmass; (**d**) deviation of the retrieved clear-sky surface pressure from its prior (ΔP_{srf}). In each panel, the mean and standard deviation (SD) of Δ_{ratio} and the number of data points (N) for each bin are presented. The results are separately plotted according to the cloud fraction (f_c) and the normalized 2 μm band radiance ($I_{2\mu m}$).

For Case 2, Δ_{ratio} is larger than that for Case 1. Although the dependence of Δ_{ratio} on Δ_{alb} is in the same direction between Cases 1 and 2, the increase in Δ_{ratio} with Δ_{alb} becomes steep, meaning that the influence of the difference in surface albedo becomes large when elevated scattering materials exist. In contrast, for Case 3, the variation trend of Δ_{ratio} with ρ_{CH4} and Δ_{alb} differs significantly from that of Cases 1 and 2. This is because clouds affected the retrieved albedo (ρ_{CH4} and Δ_{alb} increased with the increase in f_c).

3.2.3. Vertical Profile of CH_4 and CO_2

Figure 5 shows the variation of Δ_{ratio} with R_{CH4} and R_{CO2} (see Section 2.3 for the definition). The variation of Δ_{ratio} with R_{CH4} is small if the possibility of the existence of elevated scattering materials is low (Case 1). In contrast, for Case 2, Δ_{ratio} increases with the increase in R_{CH4}. This corresponds to the qualitative discussion of the influence of the CH_4 profile on Δ_{ratio} in Section 3.2.1. Although the retrieval cannot reproduce the real-world profile in detail, it is considered that the retrieved R_{CH4} represents the real-world R_{CH4} (R^{act}_{CH4}) well and can be used to explain Δ_{ratio}. In contrast to CH_4, Δ_{ratio} was expected to decrease with an increase in R_{CO2} because CO_2 is the denominator of the ratio component. However, no clear relationship between Δ_{ratio} and R_{CO2} is seen in Figure 5. Two possible reasons are considered: (1) the influence of the CO_2 profile on the ratio component is small, since R^{act}_{CO2} is smaller than R^{act}_{CH4} in general; (2) the sensitivity of the retrieval to the vertical profile for CO_2 is lower than that for CH_4 (DFS for $XCO_{2,clr}$ was 1.0–1.5 and that for $XCH_{4,clr}$ was 1.7–2.3 in the present study). When only the retrieved data having DFS for $XCO_{2,clr} \geq 1.3$ (almost half of all data) were

used, the results were not noticeably changed (Figure S5). For Case 3, the range of R_{CH4} and R_{CO2} differs from that for Cases 1 and 2, since R_{CH4} and R_{CO2} were affected by clouds. R_{CH4} was negatively correlated with f_c, which is considered to contribute to the increase in Δ_{ratio} with R_{CH4}. Although a variation of Δ_{ratio} with R_{CO2} was expected for Case 3, since R_{CO2} was also negatively correlated with f_c, the variation was small. The correlation between the variables (as mentioned in Sections 3.2.2 and 3.2.3) was accounted for in the variable selection for the bias correction (Section 4.2).

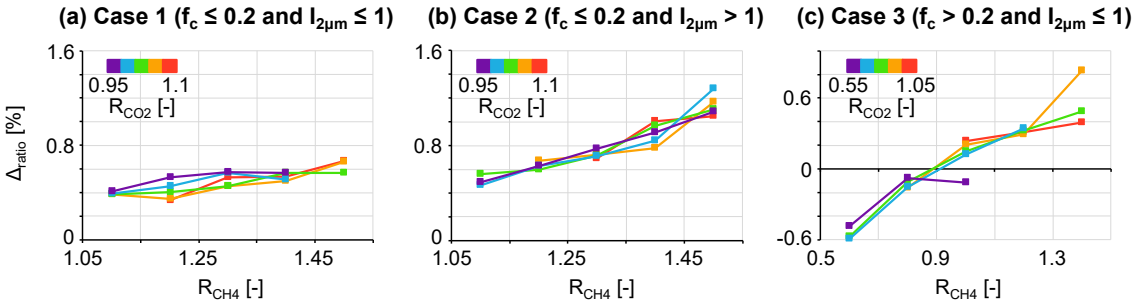

Figure 5. Variation of the relative difference in the ratio component between GOSAT and TCCON (Δ_{ratio}) according to the ratio between the partial column-averaged dry-air mole fractions for the lower atmosphere and that for the upper atmosphere (R_{CH4} and R_{CO2}): (**a**) Case 1 (the cloud fraction (f_c) ≤ 0.2 and the normalized 2 μm band radiance ($I_{2\mu m}$) ≤ 1); (**b**) Case 2 (f_c ≤ 0.2 and $I_{2\mu m}$ > 1); (**c**) Case 3 (f_c > 0.2 and $I_{2\mu m}$ ≤ 1).

4. Bias correction

4.1. Method

Linear regression was used as in many previous studies [20,37,39,72] as

$$\Delta_{ratio}^{pred} = \sum_{i=1}^{i=n} C_i x_i + C_{n+1}, \quad (3)$$

where Δ_{ratio}^{pred} is the predicted Δ_{ratio}, n is the number of variables, C_1–C_{n+1} are the regression coefficients, and x_i represents the explanatory variable. In the calculation of coefficients (least squares method), each data point (matched GOSAT and TCCON data) was weighted according to the amount of total matched GOSAT and TCCON data of the site to which the data point belonged. More specifically, the weight was given as R_{site}/N_j and $1/N_j$ for the data from sites in the northern hemisphere and that from sites in the southern hemisphere, respectively, where N_j is the total number of matched GOSAT data for each site, and R_{site} is the number of sites in the southern hemisphere divided by that in the northern hemisphere. For each GOSAT data point, the correction was calculated as

$$X_{ratio,G}^{cor} = X_{ratio,G} / \left(1 + \Delta_{ratio}^{pred}/100\right), \quad (4)$$

where $X_{ratio,G}^{cor}$ is the corrected ratio component.

4.2. Selecting Explanatory Variables

The correlation between the variables and the correlation between Δ_{ratio} and the variables were evaluated to select the variables for the bias correction (Figure 6). In Figure 6, the data with NDSI ≤ 0.4 were used to calculate the correlation coefficient with respect to f_c. Figure 6a shows that the variables were correlated with each other. In particular, f_c was highly correlated with the other variables, as mentioned in Sections 3.2.2 and 3.2.3. Therefore, the variation of Δ_{ratio} was expected to be explained by the use of fewer than the total number of variables. We confirmed that the correlation between Δ_{ratio} and the variables did not become small by the correction using one variable. Therefore, corrections

by multiple linear regression were tested. Figure 6b shows the correlation coefficient between the corrected Δ_{ratio} and the variables for the corrections using different numbers of variables. First, $I_{2\mu m}$ and airmass were used, since Δ_{ratio} varied significantly with these variables (Figures 3 and 4), and the correlation between them was low (Figure 6a). When three variables including R_{CH4} were used, the correlation coefficient became close to zero, except in the case of Δ_{alb}. This can be attributed to the fact that R_{CH4} included information on optical path length modification by scattering by clouds and aerosols. R_{CH4} is considered to be a useful variable for correcting Δ_{ratio}, although the relationship between Δ_{ratio} and R_{CH4} is somewhat empirical, especially when f_c is high.

(a) Correlation coefficient between individual variables

	$I_{2\mu m}$	f_c	ρ_{CH4}	Δ_{alb}	A_m	ΔP_{srf}	R_{CH4}	R_{CO2}
$I_{2\mu m}$		-0.09	-0.01	0.09	-0.05	-0.27	0.22	-0.13
f_c			0.43	0.33	0.30	-0.57	-0.64	-0.71
ρ_{CH4}				0.41	-0.10	-0.21	-0.29	-0.22
Δ_{alb}					0.16	-0.13	-0.17	-0.30
A_m						-0.22	-0.23	-0.24
ΔP_{srf}							0.48	0.71
R_{CH4}								0.72
R_{CO2}								

(b) Correlation coefficient between Δ_{ratio} and each variable

	$I_{2\mu m}$	f_c	ρ_{CH4}	Δ_{alb}	A_m	ΔP_{srf}	R_{CH4}	R_{CO2}
Uncorrected	0.16	-0.19	-0.07	0.07	-0.24	0.15	0.26	0.18
Corrected ($I_{2\mu m}$, A_m)		-0.10	-0.07	0.12		0.13	0.21	0.13
Corrected ($I_{2\mu m}$, A_m, R_{CH4})		0.00	0.01	0.15		0.03		-0.01
Corrected ($I_{2\mu m}$, A_m, R_{CH4}, Δ_{alb})		-0.01	-0.05			0.02		-0.01

Figure 6. Correlation coefficient (**a**) between variables and (**b**) between the relative difference in the ratio component between GOSAT and TCCON (Δ_{ratio}) and variables. The color in the figure corresponds to the coefficient value (blue: large negative coefficient; white: zero; red: large positive coefficient). The meaningless pixels are filled by gray. Eight variables were used: the normalized 2 μm band radiance ($I_{2\mu m}$), cloud fraction (f_c), retrieved surface albedo of CH_4 band (ρ_{CH4}), difference in the retrieved surface albedo (CH_4 band minus CO_2 band, Δ_{alb}), airmass (A_m), deviation of the retrieved clear-sky surface pressure from its prior (ΔP_{srf}), and ratio between the partial column-averaged dry-air mole fractions for the lower atmosphere and that for the upper atmosphere (R_{CH4} and R_{CO2}). In (**b**), results for bias-uncorrected Δ_{ratio} and bias-corrected Δ_{ratio} (corrections using two, three, and four variables) are shown. Data with $f_c = 0$ and that with $I_{2\mu m} \leq 1$ were used. Only data with NDSI ≤ 0.4 were used to calculate the correlation coefficient for f_c.

In addition to the correlation coefficient, the relationship between Δ_{ratio} and the variables was further evaluated. Figure 7 shows the variation of Δ_{ratio} with the variables. The results were separately plotted for the different hemispheres and seasons in order to confirm that the spatiotemporal variation of bias was reduced. Data with NDSI ≤ 0.4 were used to obtain the variation of Δ_{ratio} with f_c. Even when the correction was conducted using $I_{2\mu m}$ and one other variable, the difference in variation of the Δ_{ratio} with $I_{2\mu m}$ between the northern and southern hemispheres remained. Although the number of TCCON sites and the number of data points for the southern hemisphere were smaller than those for the northern hemisphere (larger standard error for the southern hemisphere), the difference in variation of the Δ_{ratio} with $I_{2\mu m}$ between hemispheres was larger than the standard error. The cause of this difference is that the degree of influence of elevated scattering materials on Δ_{ratio} varies according to the vertical profile of CH_4. When R_{CH4} was used in the correction, the difference in variation of the Δ_{ratio} with $I_{2\mu m}$ between the hemispheres was significantly reduced. For f_c, the corrected Δ_{ratio} varies around zero for both hemispheres and both seasons. For other variables, the difference between the hemispheres becomes small. Then, we decided to use the four variables airmass, $I_{2\mu m}$, R_{CH4}, and Δ_{alb} for the bias correction.

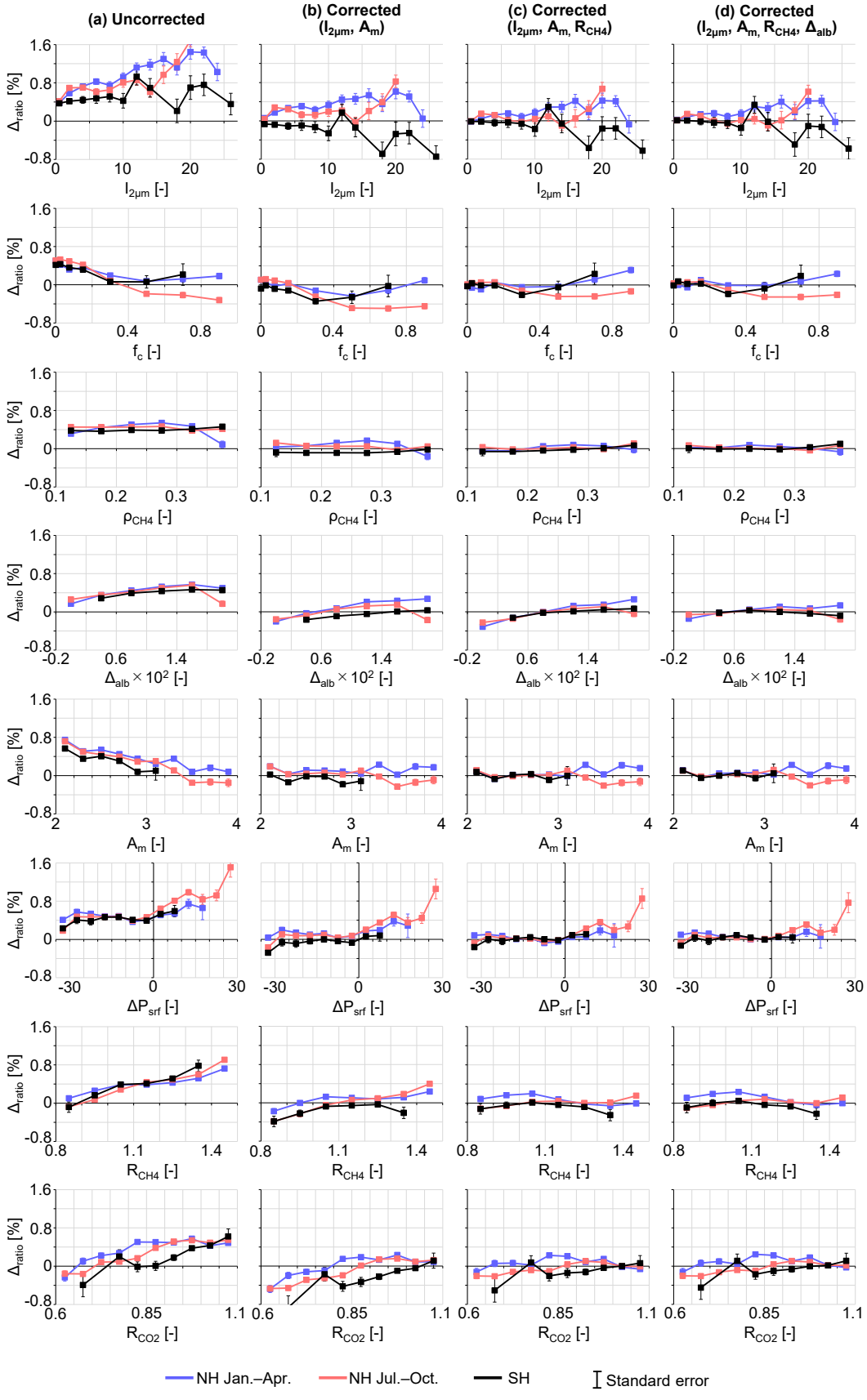

Figure 7. Variation of the relative difference in the ratio component between GOSAT and TCCON (Δ_{ratio}) according to the explanatory variables: normalized 2 μm band radiance ($I_{2\mu m}$); cloud fraction

(f_c); retrieved surface albedo of CH_4 band (ρ_{CH4}); difference in the retrieved surface albedo (CH_4 band minus CO_2 band, Δ_{alb}); airmass (A_m); deviation of the retrieved clear-sky surface pressure from its prior (ΔP_{srf}); and ratio between the partial column-averaged dry-air mole fractions for the lower atmosphere and that for the upper atmosphere (R_{CH4} and R_{CO2}). Results for (**a**) bias-uncorrected Δ_{ratio} and bias-corrected Δ_{ratio} (corrections using (**b**) two, (**c**) three, and (**d**) four variables) are presented. Results for the winter (January to April) northern hemisphere, the summer (July to October) northern hemisphere, and the southern hemisphere are plotted with different colors. Data with $f_c = 0$ and that with $I_{2\mu m} \leq 1$ were used. Only data with NDSI ≤ 0.4 were used to obtain the variation of Δ_{ratio} with f_c.

4.3. Quality Control

As quality control before evaluating the bias-corrected ratio component, cloud screening was investigated. Figure 8 shows the variation of the corrected Δ_{ratio} by the four variables according to f_c and $I_{2\mu m}$. The data with NDSI ≤ 0.4 were used. Although the data with $f_c = 0$ and those with $I_{2\mu m} \leq 1$ were used for the results shown in the previous sections (Figures 3–7), all data were used to generate Figure 8 (similar to Figure 2). Although Δ_{ratio} is close to zero for many cases where f_c is > 0 and $I_{2\mu m}$ is > 1 (i.e., data not used for the regression), the large mean and standard deviation of Δ_{ratio} remains. Therefore, the cloud screening was conducted as follows. We considered a function of f_c as $g(f_c) = (af_c + b)/(cf_c + 1)$, where *a*, *b*, and *c* are coefficients, so that the tolerance range of $I_{2\mu m}$ decreases with the increase in f_c. The coefficients were determined to make the criteria be $I_{2\mu m} \leq 15$ when $f_c = 0$ and $I_{2\mu m} \leq 1$ when $f_c = 1$, and to screen out the data in areas where the mean and/or the standard deviation of Δ_{ratio} were large in Figure 8. The criteria of $I_{2\mu m} \leq 15$ when $f_c = 0$ is based on the result that the difference in Δ_{ratio} between the hemispheres became large with the increase in $I_{2\mu m}$ (Figure 7). Then, we decided to reject the data with $I_{2\mu m} > g(f_c)$, where coefficients *a*, *b*, and *c* were 46, 15, and 60, respectively. The criteria are depicted by the white line in Figure 8.

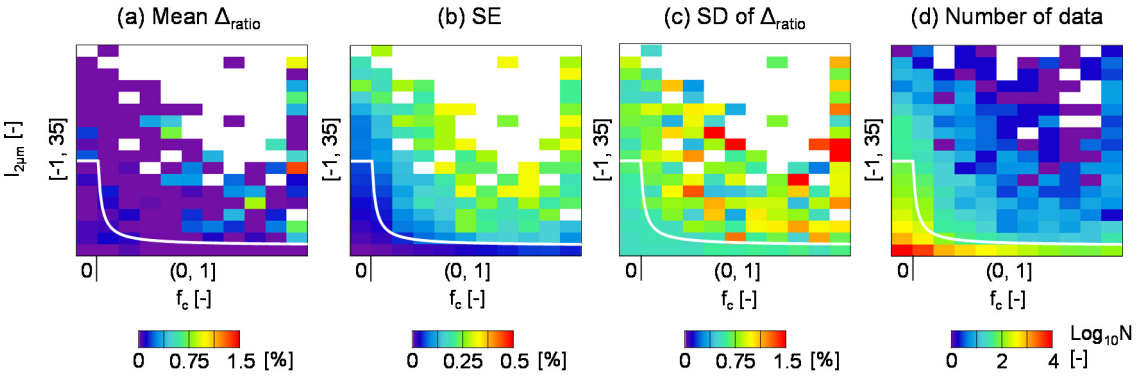

Figure 8. Similar to Figure 2, but for the bias-corrected ratio component: (**a**) mean relative difference in the ratio component between GOSAT and TCCON (Δ_{ratio}); (**b**) standard error (SE); (**c**) standard deviation (SD) of Δ_{ratio}; (**d**) number of data points. The white line indicates the cloud screening criterion.

4.4. Evaluating the Corrected Results

To examine the usefulness and applicability of the bias correction, the matched GOSAT and TCCON data acquired in the even-numbered years were used to obtain the regression coefficients, and then the correction was applied to the GOSAT data acquired in the odd-numbered years. The obtained coefficients for airmass, $I_{2\mu m}$, R_{CH4}, and Δ_{alb} and the intercept were −0.28, 0.019, 1.06, 17.69, and −0.31, respectively (note that the four variables are dimensionless; see Section 2.3 for the definition of the variables). The cloud screening described in Section 4.3 was conducted. Figure 9 shows the comparison of the bias, precision, and interseasonal bias for each TCCON site between the bias-uncorrected and the bias-corrected ratio component. After the bias correction, the interseasonal bias was reduced, and the variation between sites in the northern hemisphere and the difference

between hemispheres became small. The precision and intersite bias were also improved. The reduction of precision value was statistically significant ($p < 0.001$ from F test). The reduction of intersite bias value was less significant, but the 75% confidence intervals (CI) showed almost no overlap (0.177–0.234% and 0.143–0.179% for before and after the bias correction, respectively). The CI of intersite bias was estimated by the nonparametric bootstrap method. For each site, a bootstrap sample was taken, and a bootstrap estimate of bias (mean Δ_{ratio} of the sample) was obtained. Then, the intersite bias (standard deviation of the estimated bias values for individual sites) was calculated. This calculation was repeated 2000 times, and the CI was obtained from the 2000 intersite bias values.

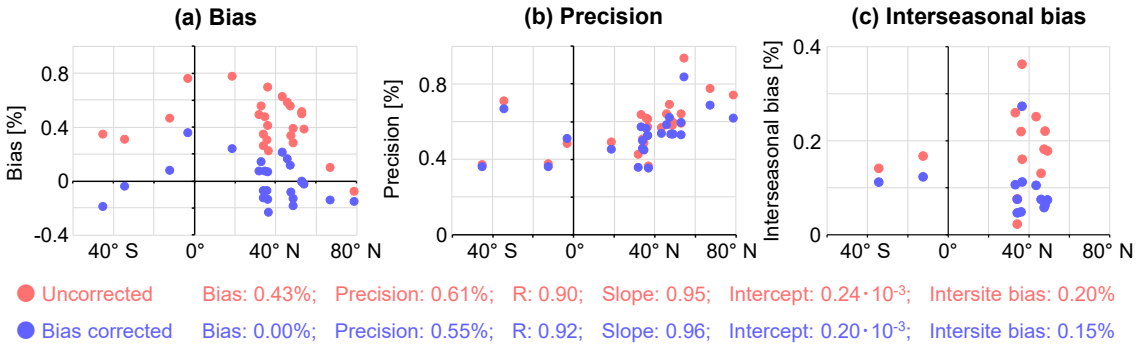

Figure 9. Latitudinal plot of (**a**) the bias, (**b**) precision, and (**c**) interseasonal bias of the uncorrected and the bias-corrected GOSAT ratio component for each TCCON site. Only sites having more than nine data points are shown. The bias, precision, correlation coefficient (R), and the slope and intercept of the linear regression calculated using all data (in a manner similar to Figure 1a) are presented below the graphs.

Figure 10 shows the temporal variation of the uncorrected and corrected Δ_{ratio} for each TCCON site. The results for TCCON sites with long-term observation and a large number of data points are shown. For other sites, it was difficult to discuss the temporal variation of Δ_{ratio}, but no results contradicting the following discussion were obtained. On the whole, seasonality was seen for the uncorrected Δ_{ratio}, but it was significantly reduced by the correction. Δ_{ratio} was small even before the correction for the high-latitude site (Sodankylä [73]). Such a general seasonal and latitudinal pattern of Δ_{ratio} seems to be caused by the airmass dependence of Δ_{ratio} (Figure 4). In addition to this general pattern, the characteristics of each site were observed as described below. For each site, the temporal variation of Δ_{ratio} was determined as follows: the mean Δ_{ratio} was calculated for each season (DJF, MAM, JJA, SON) in each year (four seasons × five years), and then the mean and the standard deviation of the mean Δ_{ratio} values were calculated (Figure 11). For comparison, results for the corrected Δ_{ratio} with two and three variables are also shown.

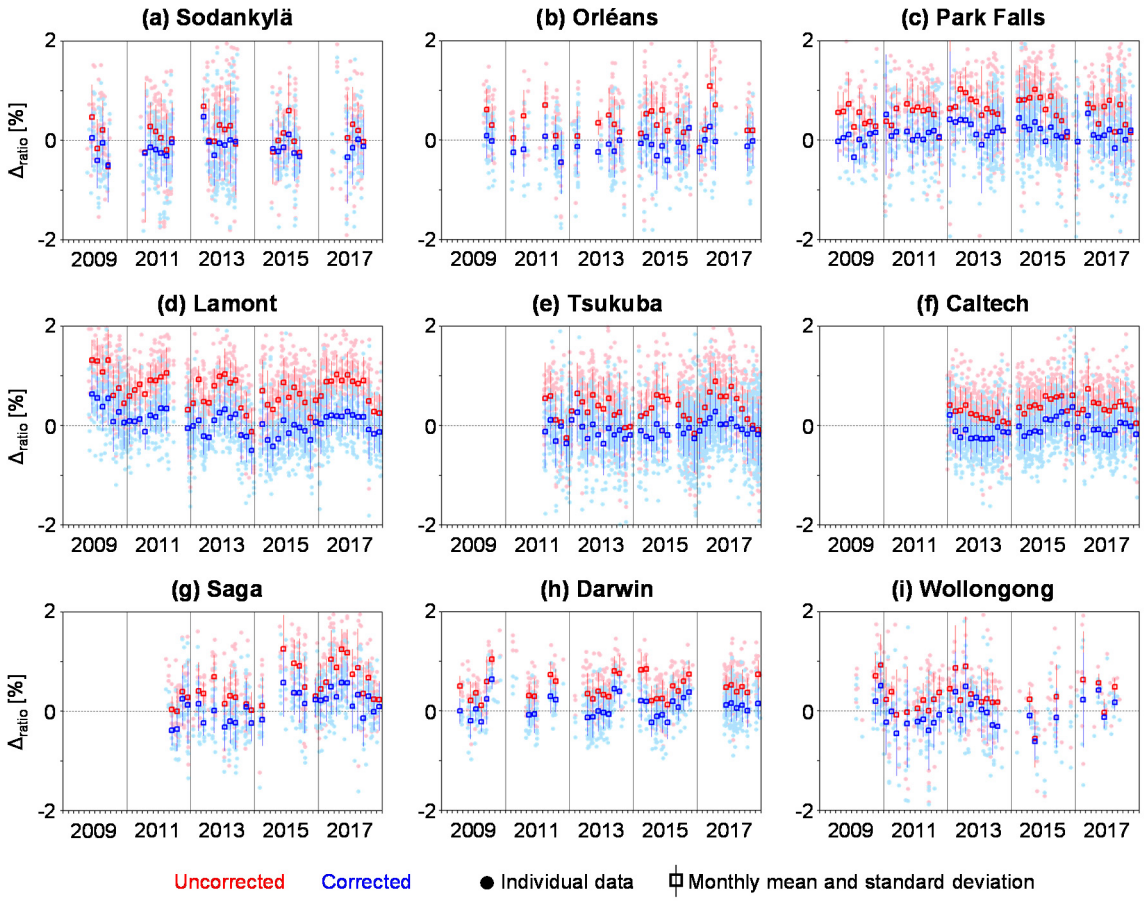

Figure 10. Temporal variation of the relative difference in the ratio component between GOSAT (bias-uncorrected and bias-corrected) and TCCON (Δ_{ratio}) for each TCCON site: (**a**) Sodankylä; (**b**) Orléans; (**c**) Park Falls; (**d**) Lamont; (**e**) Tsukuba; (**f**) Caltech; (**g**) Saga; (**h**) Darwin; (**i**) Wollongong. Individual data and monthly mean are plotted. Results for the data acquired in the odd-numbered years are shown to assess the applicability of the bias correction using the independent data (coefficients for the correction were obtained using the data acquired in the even-numbered years).

(a) Mean Δ_{ratio} [%]

	Uncorrected	Corrected ($I_{2\mu m}$, A_m)	Corrected ($I_{2\mu m}$, A_m, R_{CH4})	Corrected ($I_{2\mu m}$, A_m, R_{CH4}, Δ_{alb})
Sodankylä	0.07	-0.20	-0.15	-0.13
Orléans	0.33	0.02	-0.08	-0.10
Park Falls	0.58	0.25	0.18	0.18
Lamont	0.63	0.21	0.07	-0.01
Tsukuba	0.35	-0.06	-0.15	-0.07
Caltech	0.34	-0.05	-0.16	-0.06
Saga	0.56	0.12	0.07	0.14
Darwin	0.50	-0.01	0.06	0.09
Wollongong	0.27	-0.14	-0.11	-0.09

(b) SD of Δ_{ratio} [%]

Uncorrected	Corrected ($I_{2\mu m}$, A_m)	Corrected ($I_{2\mu m}$, A_m, R_{CH4})	Corrected ($I_{2\mu m}$, A_m, R_{CH4}, Δ_{alb})
0.11	0.10	0.07	0.07
0.25	0.14	0.11	0.10
0.22	0.16	0.14	0.13
0.20	0.16	0.17	0.16
0.23	0.15	0.11	0.11
0.12	0.13	0.13	0.13
0.32	0.28	0.23	0.23
0.19	0.15	0.14	0.16
0.20	0.19	0.19	0.19

Figure 11. (**a**) Mean and (**b**) standard deviation (SD) of the mean values of relative difference in the ratio component between GOSAT and TCCON (Δ_{ratio}) calculated for individual seasons (each season in each year) for each TCCON site. Results for the bias-uncorrected and bias-corrected ratio component (corrections using two, three, and four variables) are presented. The color in the figure corresponds to the Δ_{ratio} value (blue: large negative value; white: zero; red: large positive value) and the SD value (blue: zero; red: large value) for the mean and SD, respectively.

For Sodankylä, the uncorrected Δ_{ratio} was smaller than that for the other sites owing to the large airmass. The low possibility of elevated scattering materials ($I_{2\mu m}$ was small for most of the data) also seems to have contributed to the small Δ_{ratio}. Δ_{ratio} was overcorrected by the correction using two variables. f_c tended to be high for the data over this site, and R^{act}_{CH4} seemed to be large according to the model (prior value). Then, the overcorrection was reduced by using four variables. For Orléans, occasional large $I_{2\mu m}$, in addition to the airmass effect, seemed to cause a large standard deviation; however, the deviation decreased after the correction. For Park Falls, the uncorrected Δ_{ratio} was considered to be affected by many factors. The temporal variation of Δ_{alb} was large, since this site was covered by snow during winter and by vegetation during summer. Large $I_{2\mu m}$ was observed during spring. R^{act}_{CO2} is expected to be small during summer due to photosynthesis by vegetation. R^{act}_{CH4} seemed to be large during summer according to the model (prior value). Correction using R_{CH4} reduced Δ_{ratio}, although a relatively large Δ_{ratio} remained, since the complicated conditions were not perfectly accounted for by the correction. For Lamont, large Δ_{alb} generally brought large Δ_{ratio}. The correction using Δ_{alb} reduced Δ_{ratio}. A large uncorrected Δ_{ratio} was occasionally seen in the early months of the year (Figure 10). We found that the large Δ_{ratio} corresponded to the large $I_{2\mu m}$ in February 2013 and 2017. According to Figure 10, these large errors were properly corrected. The use of $I_{2\mu m}$ in the correction had only a small effect on the averaged results (Figure 11), since $I_{2\mu m}$ was not always large; however, the effect could be confirmed for individual cases. For Tsukuba, a large $I_{2\mu m}$ was observed during spring to summer, which enhanced the seasonality of the uncorrected Δ_{ratio}. Δ_{alb} of this site was small, and thus the overcorrection was reduced by using Δ_{alb} in the correction. For Caltech, Δ_{alb} was small, and the temporal variations of R^{act}_{CH4} and R^{act}_{CO2} were small according to the model. The difference between R^{act}_{CH4} and R^{act}_{CO2} was also small. Then, the uncorrected Δ_{ratio} showed small temporal variation, and the corrected Δ_{ratio} varied around zero with the small temporal variation retained. For Saga, the airmass effect and the large $I_{2\mu m}$ during spring to summer enhanced the seasonality, and Δ_{ratio} was significantly reduced by the correction using two variables. The temporal variation of R^{act}_{CH4} was expected to be large according to the model. Thus, using R_{CH4} in the correction improved both the mean and standard deviation (Figure 11). For the sites in the southern hemisphere (Darwin and Wollongong), although R^{act}_{CH4} and R^{act}_{CO2} were expected to be small, the amplitude of temporal variation of uncorrected Δ_{ratio} was comparable to that for the sites in the northern hemisphere (Figure 10). For Darwin, the uncorrected Δ_{ratio} showed large temporal variation, although the variation of airmass was small. For Wollongong, occasional large uncorrected Δ_{ratio} did not correspond to the large $I_{2\mu m}$. The standard deviation was reduced only slightly by the correction for these sites (Figure 11). Although using R_{CH4} in the correction reduced the difference between the northern and southern hemispheres (Figure 7), unaccounted factors might remain. On the whole, the optimal variables differ between sites; but the correction using four variables brought the best result in terms of the balance between sites (the mean of absolute Δ_{ratio} values for individual sites was close to zero and the variation between sites was small).

We also conducted a bias correction for the data acquired with gain M using the four variables and the above-mentioned coefficients (i.e., the coefficients were obtained using the gain H data). The bias correction functioned properly for the gain M data, although the bias was small even for the uncorrected data (Appendix B). This result supports the applicability of the bias correction.

5. Conclusions

The relationship between the bias in the GOSAT ratio component and the variables derived from GOSAT data was investigated, and the bias correction and its evaluation were performed. The bias between the uncorrected GOSAT ratio component and the TCCON ratio component was 0.43% when the cloud-free condition was expected (normalized 2 μm band radiance ($I_{2\mu m}$) ≤ 1 and cloud fraction (f_c) = 0). The bias increased with the increase in $I_{2\mu m}$ and reached 1.5% when $I_{2\mu m}$ was 30. The variation of bias with f_c was small when f_c was small or large (the bias was 0.4% to 0.5% for the data with $f_c \leq 0.2$ and −0.1% to 0% for the data with $f_c \geq 0.4$). The variation of bias according to $I_{2\mu m}$ and f_c

could be interpreted based on the difference in the detection target between $I_{2\mu m}$ and f_c, the difference in surface albedo between the CH_4 and CO_2 bands (Δ_{alb}), and the vertical profile of CH_4 and CO_2. The relationship between the bias and other related variables was also investigated. We used the retrieved profile and the ratios between the upper and lower atmosphere CH_4 and CO_2 (R_{CH4} and R_{CO2}), in addition to the variables that have been used in the bias correction for the full-physics method (airmass) and in the cloud screening (deviation of the retrieved clear-sky surface pressure from its prior (ΔP_{srf})) and that have been revealed to be a large error source for the proxy method (Δ_{alb}). The bias showed clear variations with the variables except for R_{CO2}.

Then, airmass, $I_{2\mu m}$, R_{CH4}, and Δ_{alb} were selected as explanatory variables for a linear regression of the bias by considering the correlation between the variables and the correlation between the variables and the bias. Using R_{CH4} in the correction reduced the dependence of the bias on f_c and ΔP_{srf}. The difference in bias between the northern and the southern hemispheres was also reduced. These results are attributed to the information on the CH_4 vertical profile and the effect of atmospheric scattering included in R_{CH4}. Although the relationship between bias and R_{CH4} is somewhat empirical, R_{CH4} is an important variable for correcting the bias in the ratio component. Before evaluating the corrected results, cloud screening was applied. The criteria were determined as the threshold value of $I_{2\mu m}$ decreases with the increase in f_c ($I_{2\mu m} \leq 15$ when $f_c = 0$ and $I_{2\mu m} \leq 1$ when $f_c = 1$), by investigating the variation of bias in the corrected ratio component with f_c and $I_{2\mu m}$. Although f_c and $I_{2\mu m}$ have been used for the cloud screening of the GOSAT proxy retrievals, our results give a quantitative basis for the screening.

Comparison between the corrected ratio component and TCCON showed that the precision (standard deviation of the difference between GOSAT and TCCON) was reduced from 0.61% to 0.55%, and the intersite bias was reduced from 0.20% to 0.15%. The temporal variation of bias was further investigated for the sites having a long-term record and a large amount of data. The uncorrected bias showed a seasonality with a large bias in summer. The difference in monthly mean bias between summer and winter exceeded 1% for several sites. In addition to such seasonality, the months with a large mean bias corresponded to the months with a large mean $I_{2\mu m}$. The temporal variation of bias was significantly reduced by the correction. Although the optimal variables differed between sites, the mean and standard deviation of the mean bias values for individual seasons (each season in each year) were within 0.2% for most of the sites, when the four variables were used for the correction.

The bias-corrected and cloud-screened ratio component data in the present study reduce the concern that the residual errors related to the atmospheric scattering and the property of ground surfaces affect the inverse modeling of CH_4 sources and sinks. In future work, the impact of utilizing the bias-corrected data in the inverse modeling will be investigated. GOSAT has been operating for more than 10 years. GOSAT-2, a successor mission to the GOSAT, was launched on 29 October 2018. Providing long-term, consistent, and high-quality XCH_4 data set by the GOSAT series is expected to contribute to the studies on CH_4 budgets over the globe. To construct such a data set, GOSAT and GOSAT-2 data will be continuously compared with each other and with the data from other satellites and TCCON.

Supplementary Materials: The following are available online at http://www.mdpi.com/2072-4292/12/19/3155/s1, Figure S1: Relationship among the Normalized Difference Snow Index (NDSI), relative difference in the ratio component between GOSAT and TCCON (Δ_{ratio}), and month of observation. Figure S2: Averaging kernel of the GOSAT clear-sky retrieval for (a) XCH_4 and (b) XCO_2 (monthly mean values of GOSAT data matched the TCCON data). Figure S3: Similar to Figure 1, but for the data with TCCON Fractional Variation in Solar Intensity (FVSI) ≤ 1% and the data with FVSI > 1%. Figure S4: Relationship between the relative difference in the ratio component between GOSAT and TCCON (Δ_{ratio}) and the TCCON Fractional Variation in Solar Intensity (FVSI). Figure S5: Similar to Figure 5, but using GOSAT data with DFS for $XCO_2 \geq 1.3$.

Author Contributions: Conceptualization, Y.Y.; methodology, H.O. (Haruki Oshio) and Y.Y.; software, H.O. (Haruki Oshio) and Y.Y.; validation, H.O. (Haruki Oshio); formal analysis, H.O. (Haruki Oshio) and Y.Y.; investigation, H.O. (Haruki Oshio); resources, T.M., N.M.D., M.D., D.W.T.G., F.H., L.T.I., R.K., C.L., I.M., J.N., Y.-S.O., H.O. (Hirofumi Ohyama), C.P., D.F.P., C.R., K.S., R.S., Y.T., V.A.V., T.W., and D.W.; data curation, Y.Y. and T.M.; writing—original draft preparation, H.O. (Haruki Oshio); writing—review and editing, all; visualization,

H.O. (Haruki Oshio); supervision, Y.Y.; project administration, T.M.; funding acquisition, T.M. All authors have read and agreed to the published version of the manuscript.

Funding: The Garmisch TCCON station has been supported by the European Space Agency (ESA) under grant 4000120088/17/I-EF and by the German Bundesministerium für Wirtschaft und Energie (BMWi) via the Deutsche Zentrum für Luft- und Raumfahrt (DLR) under grant 50EE1711D. TCCON stations at Tsukuba, Rikubetsu and Burgos are supported in part by the GOSAT series project. Burgos is also partially supported by the Energy Development Corp, Philippines. Darwin and Wollongong TCCON sites and NMD are supported by Australian Research Council funding via FT180100327, DP160101598, DP140101552, DP110103118, DP0879468 and LE0668470 and NASA grants NAG5-12247 and NNG05-GD07G and the University of Wollongong. The Paris TCCON site has received funding from Sorbonne Université, the French research center CNRS, the French space agency CNES, and Région Île-de-France.

Acknowledgments: GOSAT clear-sky retrieval in the present study was conducted at the GOSAT-2 Research Computation Facility.

Conflicts of Interest: The authors declare no conflict of interest.

Appendix A. TCCON Sites and the Influence of the Matching Criteria of GOSAT and TCCON

We used TCCON data from 26 sites [41–67]. Figure A1 shows the map of TCCON sites, and Table A1 shows an overview of the sites. Basically, the sites are located in areas with relatively uniform surface properties and are reasonably far from anthropogenic sources. However, several sites are in areas with nonflat topography or are located near or in urban areas. Such characteristics are summarized in the rightmost column of Table A1.

In the main text, GOSAT data within a ±2° latitude/longitude box centered at each TCCON site were used for the comparison. The influence of the matching criteria on the analysis was assessed. Table A2 shows the mean and standard deviation of Δ_{ratio} for each TCCON site. Results for the different matching criteria are tabulated. The mean value showed almost no clear trend, but the deviation value decreased as the matching criteria were tightened. Figure A2 shows the relationship between Δ_{ratio} and the related variables for the matching criteria of ±2° and that of ±0.5°. Although more deviated values are seen for the matching criteria of ±2°, the regression lines were similar between the criteria. The mean Δ_{ratio} values for the bins also show similar trends between the criteria (Figure A3). The skewness around 0 indicates the small asymmetry for the distribution of Δ_{ratio} values for each bin. Large negative kurtosis values were hardly seen, meaning there was no high frequency for either side (large and small Δ_{ratio}).

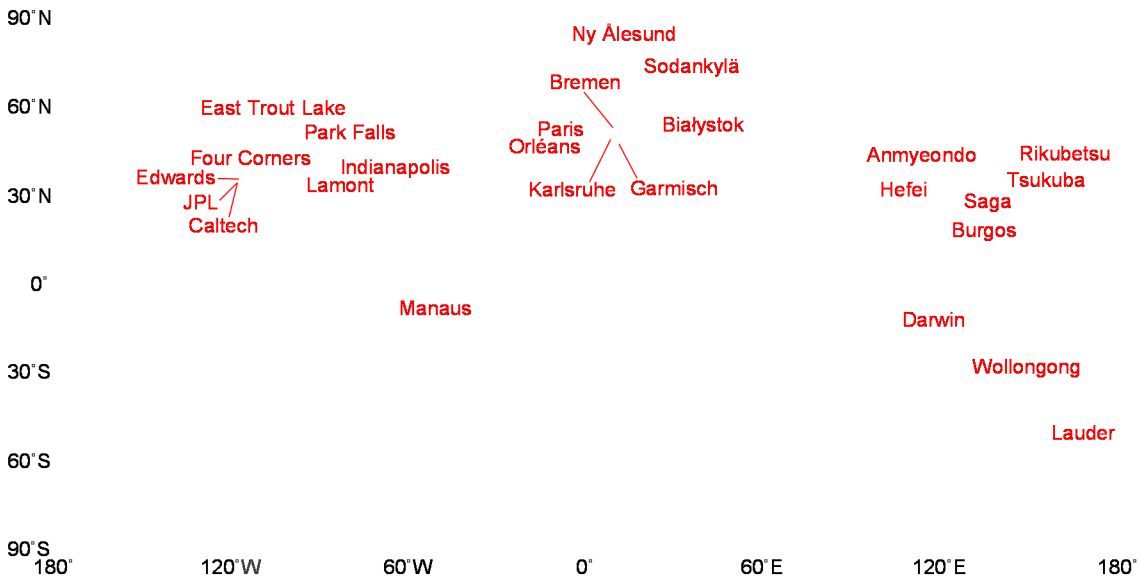

Figure A1. Map of the TCCON sites used.

Table A1. Overview of the TCCON sites used.

Site	Country	Latitude (deg.)	Longitude (deg.)	Altitude(km)	Observation Period of the Data Used	Specific Characteristics
Ny Ålesund	Spitzbergen, Norway	78.92N	11.92E	0.02	6 April 2014–31 December 2018	Useful data are not obtained during winter due to the high solar zenith angle.
Sodankylä	Finland	67.37N	26.63E	0.19	16 May 2009–31 December 2018	Useful data are not obtained during winter due to the high solar zenith angle.
East Trout Lake	Canada	54.35N	104.99W	0.50	7 October 2016–31 December 2018	
Bialystok	Poland	53.23N	23.03E	0.18	23 April 2009–1 October 2018	
Bremen	Germany	53.10N	8.85E	0.03	22 January 2010–31 December 2018	The site is in the middle-sized city (population ~550 000).
Karlsruhe	Germany	49.10N	8.44E	0.12	19 April 2010–31 December 2018	The site is near the middle-sized city (population ~300 000).
Paris	France	48.85N	2.36E	0.06	23 September 2014–31 December 2018	The site is in the large city (population ~2.15 million).
Orléans	France	47.97N	2.11E	0.13	29 August 2009–31 December 2018	
Garmisch	Germany	47.48N	11.06E	0.74	23 April 2009–31 December 2018	
Park Falls	USA	45.95N	90.27W	0.44	23 April 2009–31 December 2018	
Rikubetsu	Japan	43.46N	143.77E	0.38	16 November 2013–31 December 2018	
Indianapolis	USA	39.86N	86.00W	0.27	23 August 2012–1 December 2012	The site is in the suburban area of a middle-sized city (population ~880 000).
Four Corners	USA	36.80N	108.48W	1.64	16 March 2013–4 October 2013	The site is far from the city area but observes plant plumes and methane from mine shafts and fugitive leaks [74,75]. The observed total column peaks in the late morning.
Lamont	USA	36.60N	97.49W	0.32	23 April 2009–31 December 2018	
Anmyeondo	Korea	36.54N	126.33E	0.03	2 February 2015–18 April 2018	The site is located on the west coast of the Korean Peninsula.
Tsukuba	Japan	36.05N	140.12E	0.03	4 August 2011–31 December 2018	The site is in the middle-sized city (population ~240 000).
Edwards	USA	34.96N	117.88W	0.70	20 July 2013–31 December 2018	The site is adjacent to a very bright playa.
JPL	USA	34.20N	118.18W	0.39	19 May 2011–14 May 2018	The site is near the large city (population ~17 million).
Caltech	USA	34.14N	118.13W	0.23	20 September 2012–31 December 2018	The site is near the large city (population ~17 million).

Table A1. *Cont.*

Site	Country	Latitude (deg.)	Longitude (deg.)	Altitude(km)	Observation Period of the Data Used	Specific Characteristics
Saga	Japan	33.24N	130.29E	0.01	28 July 2011–31 December 2018	The site is in the middle-sized city (population ~230 000).
Hefei	China	31.91N	117.17E	0.03	18 September 2015–31 December 2016	The site is near the large city (population ~5 million).
Burgos	Philippines	18.53N	120.65E	0.04	3 March 2017–31 December 2018	The site is at the northernmost point of Luzon Island in the Philippines.
Manaus	Brazil	3.21S	60.60W	0.05	1 October 2014–24 June 2015	
Darwin	Australia	12.42S	130.89E	0.03	23 April 2009–31 December 2018	
Lauder	New Zealand	45.04S	169.68E	0.37	23 April 2009–31 December 2018	The site is in the midst of rolling hills.
Wollongong	Australia	34.41S	150.88E	0.03	23 April 2009–31 December 2018	The site is between the ocean and a sharp escarpment.

Table A2. Mean (μ) and standard deviation (SD) of the relative difference in the ratio component between GOSAT and TCCON and the number of matched GOSAT and TCCON data points (N) for each TCCON site. Results for four different matching criteria are shown: GOSAT data within ±2°, ±1°, ±0.5°, and ±0.1° latitude/longitude boxes centered at each TCCON site. Only sites having more than 29 data points are shown. The GOSAT data obtained under conditions where cloud-free scenes were expected (cloud fraction = 0 and normalized 2 μm band radiance ≤ 1) were used. Intersite bias is calculated using the same sites as in the case of matching criteria of ±0.1°.

	±2°			±1°			±0.5°			±0.1°		
Site	**μ (%)**	**SD (%)**	**N**	**μ (%)**	**SD (%)**	**N**	**μ (%)**	**SD (%)**	**N**	**μ (%)**	**SD (%)**	**N**
Sodankylä	0.43	0.74	328	0.26	0.85	88						
East Trout Lake	0.57	0.68	40									
Bialystok	0.50	0.56	263	0.46	0.51	87	0.53	0.45	50			
Bremen	0.51	0.54	81									
Karlsruhe	0.22	0.62	267	0.19	0.57	102						
Paris	0.43	0.52	102	0.50	0.50	59						
Orléans	0.35	0.51	518	0.35	0.51	224	0.43	0.52	75			
Garmisch	0.55	0.61	286	0.53	0.56	184	0.54	0.52	56			
Park Falls	0.61	0.55	1017	0.61	0.55	728	0.59	0.55	575	0.60	0.55	536
Rikubetsu	0.63	0.46	135	0.73	0.44	56						
Indianapolis	0.44	0.64	67									
Lamont	0.59	0.54	1949	0.59	0.51	855	0.61	0.45	461	0.62	0.45	305
Anmeyondo	0.51	0.45	50	0.52	0.37	33						
Tsukuba	0.31	0.61	1407	0.31	0.59	1186	0.28	0.60	675	0.41	0.49	179
Edwards	0.43	0.45	126	0.60	0.45	59						
JPL	0.26	0.49	609	0.27	0.43	490	0.24	0.39	438	0.25	0.38	103
Caltech	0.32	0.43	2067	0.32	0.43	1924	0.32	0.43	1412	0.31	0.43	853
Saga	0.59	0.59	438	0.58	0.55	288	0.65	0.53	222	0.72	0.52	66
Darwin	0.37	0.36	555	0.38	0.36	500	0.56	0.36	46	0.48	0.34	30
Wollongong	0.42	0.71	349	0.31	0.58	195	0.34	0.61	100			
Lauder	0.36	0.35	124	0.35	0.34	121	0.37	0.31	92	0.36	0.30	85
All sites	0.43	0.55	10846	0.41	0.52	7263	0.40	0.51	4357	0.45	0.49	2249
Intersite bias	0.14			0.13			0.16			0.15		

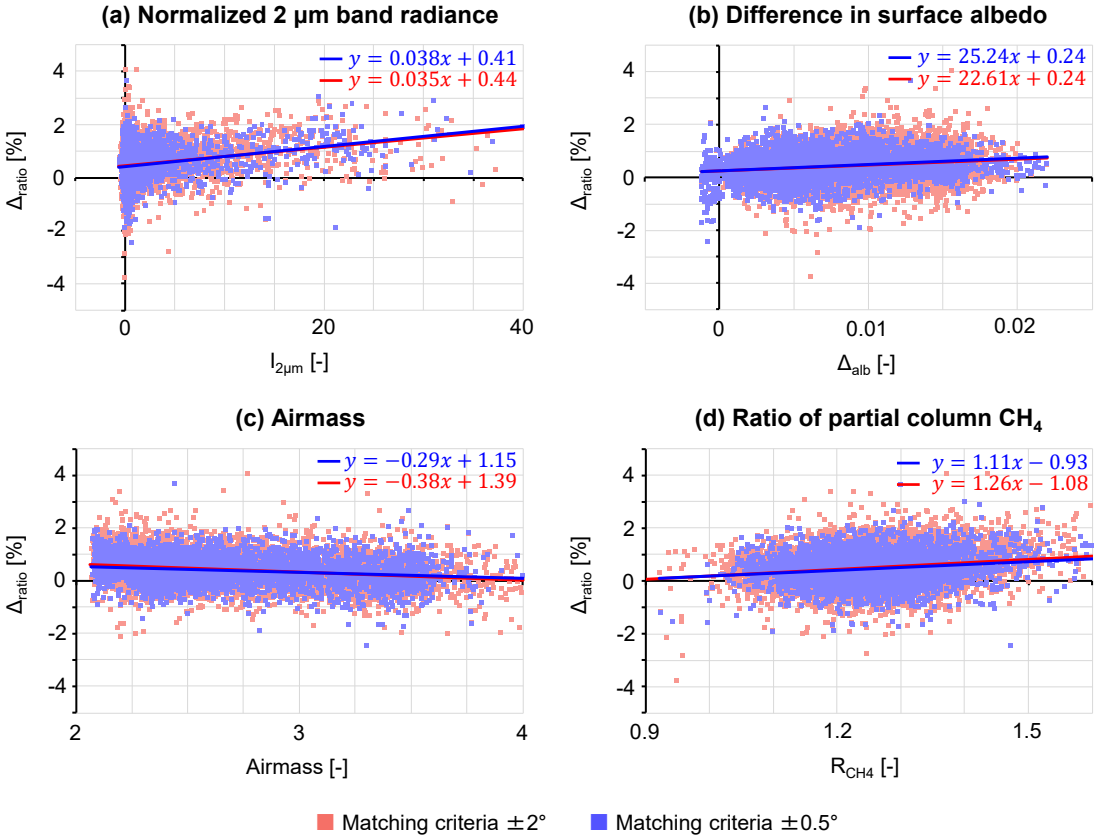

Figure A2. Relationship between the relative difference in the ratio component between GOSAT and TCCON (Δ_{ratio}) and the related variable: (**a**) normalized 2μm band radiance ($I_{2\mu m}$); (**b**) difference in retrieved surface albedo (CH_4 band minus CO_2 band, Δ_{alb}); (**c**) airmass; (**d**) ratio between the partial column-averaged dry-air mole fractions for the lower atmosphere and that for the upper atmosphere (R_{CH4}). Results for the different matching criteria are plotted (GOSAT data within ±2° and ±0.5° latitude/longitude boxes centered at each TCCON site). Linear regressions are depicted by solid lines. For $I_{2\mu m}$ and R_{CH4}, the data with cloud fraction = 0 were used. For Δ_{alb} and airmass, the data with cloud fraction = 0 and $I_{2\mu m} \leq 1$ were used.

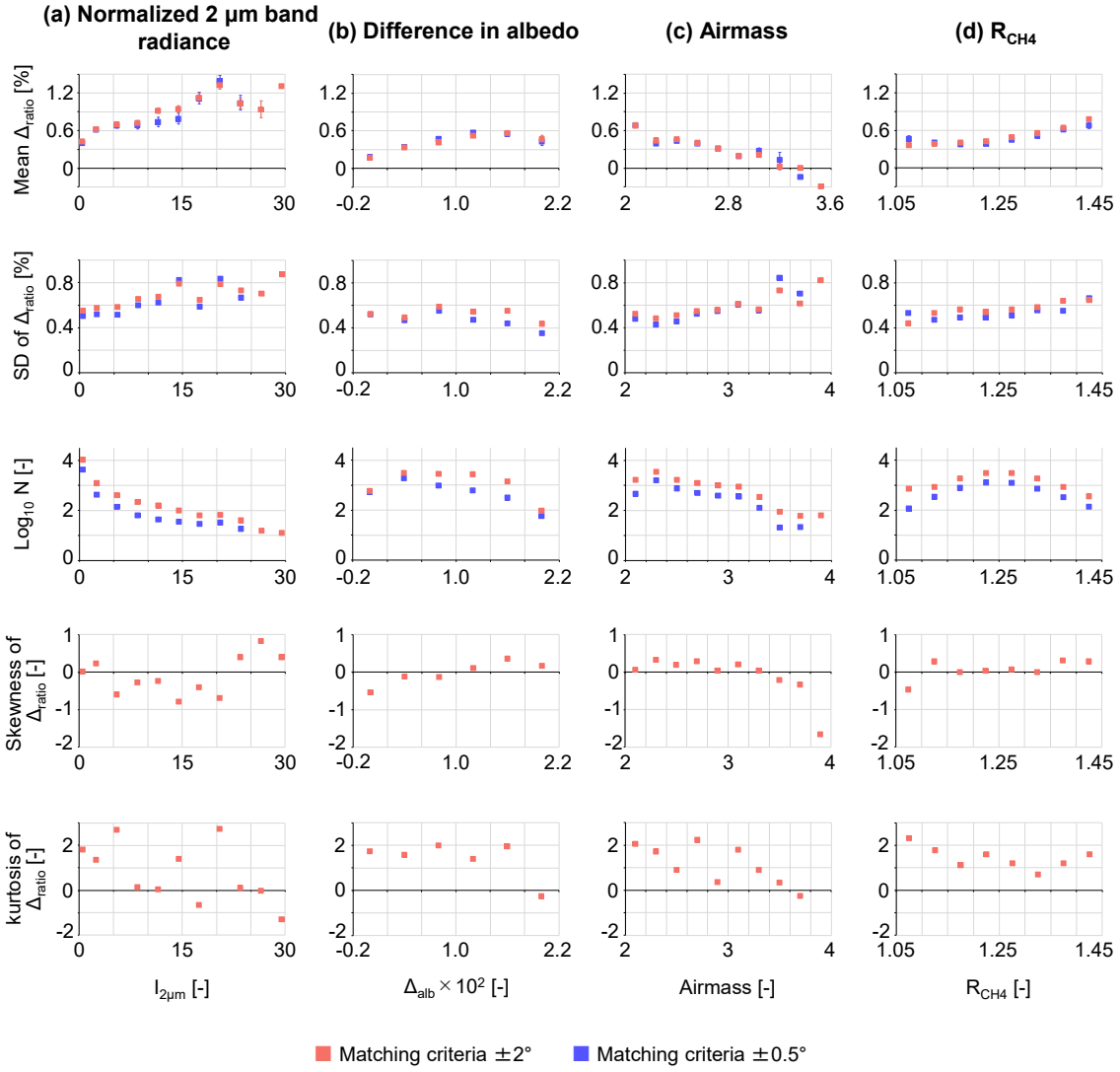

Figure A3. Relationship between the relative difference in the ratio component between GOSAT and TCCON (Δ_{ratio}) and the related variables. The variables (**a**–**d**) are similar to those in Figure A2, but in each panel, the mean and standard deviation (SD) of Δ_{ratio}, number of data points (N), skewness, and kurtosis for each bin are shown. Results for the different matching criteria are plotted (GOSAT data within ±2° and ±0.5° latitude/longitude boxes centered at each TCCON site). For $I_{2\mu m}$ and R_{CH4}, the data with cloud fraction = 0 were used. For Δ_{alb} and airmass, the data with cloud fraction = 0 and $I_{2\mu m} \leq 1$ were used.

Appendix B. Bias Correction for the Data Acquired by Gain M

The different gain settings of the TANSO-FTS (H and M) only affect the spectral radiance of the Band 1 [76]. Therefore, the ratio component should show similar characteristics between the data acquired with gain H and that acquired with gain M. Then, the bias correction equation established using the gain H data (four variables with the coefficients shown in Section 4.4) was applied to the gain M data. Figure A4 shows the scatterplot of the ratio component derived from GOSAT gain M data and that derived from TCCON. The results for each site are shown in Table A3. The bias-uncorrected and bias-corrected results are presented in the left and right sides in Figure A4 and Table A3, respectively. Figure A5 shows the dependence of Δ_{ratio} on the related variables for the uncorrected and the corrected data. The matching criteria were similar to those in the main text. Only GOSAT data over the areas east of 118°W were used to reject the data over Bakersfield where there are oil fields. According to

Figure A4, the bias was smaller than that for the gain H data for the uncorrected data, and the bias was slightly overcorrected. Table A3 shows that the overcorrection was seen for the data of JPL and Caltech. This is reasonable for the following reasons. Almost all the GOSAT data acquired with gain M in this region were located around the Edwards site. For the time period during which TCCON observation was not being performed at the Edwards site, the GOSAT data were matched with the TCCON data at JPL or Caltech. The Edwards site is located in the north of San Gabriel Mountains, while the other two sites are located in the south of the mountains. Therefore, it was possible that the air at the other two sites was occasionally different from the air at the Edwards site. Then, the results for the Edwards site (bias of −0.07% after the correction) indicate that the GOSAT data can be used for the proxy retrieval without exercising caution with respect to the gain settings and support the applicability of the bias correction.

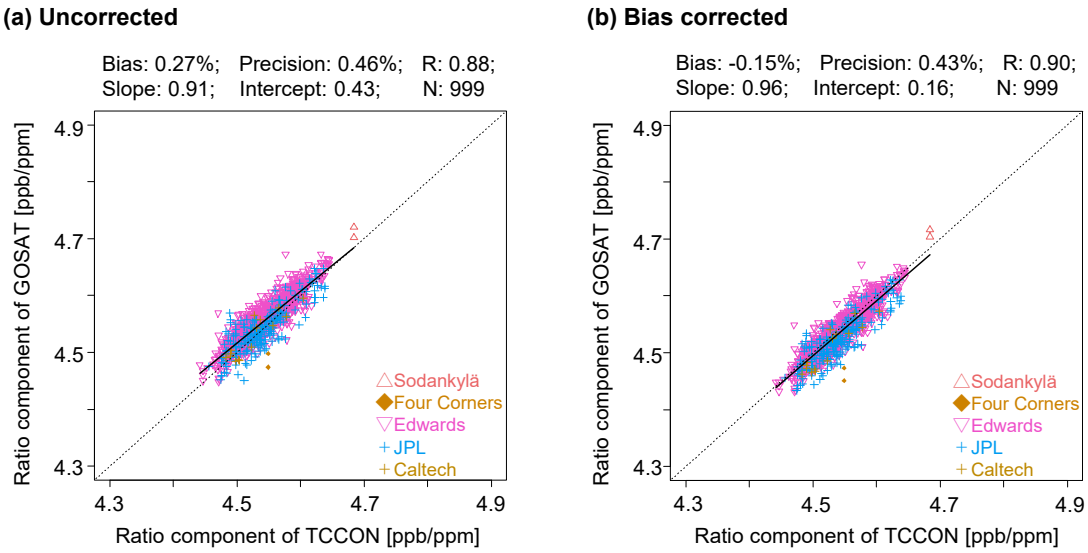

Figure A4. Similar to Figure 1a but for GOSAT data acquired with gain M: (**a**) bias-uncorrected; (**b**) bias-corrected.

Table A3. The relative difference in the ratio component between GOSAT (gain M) and TCCON (Δ_{ratio}) for each site: mean (μ), standard deviation (SD), and interseasonal bias (S_{SD}) of Δ_{ratio} and the number of matched GOSAT and TCCON data points (N) are shown.

	Uncorrected				Bias-Corrected			
Site	**μ (%)**	**SD (%)**	**S_{SD} (%)**	**N**	**μ (%)**	**SD (%)**	**S_{SD} (%)**	**N**
Edwards	0.35	0.41	0.11	766	−0.07	0.39	0.04	766
JPL	0.01	0.50	0.11	214	−0.39	0.46	0.09	214
Caltech	0.04	0.35		15	−0.40	0.34		15

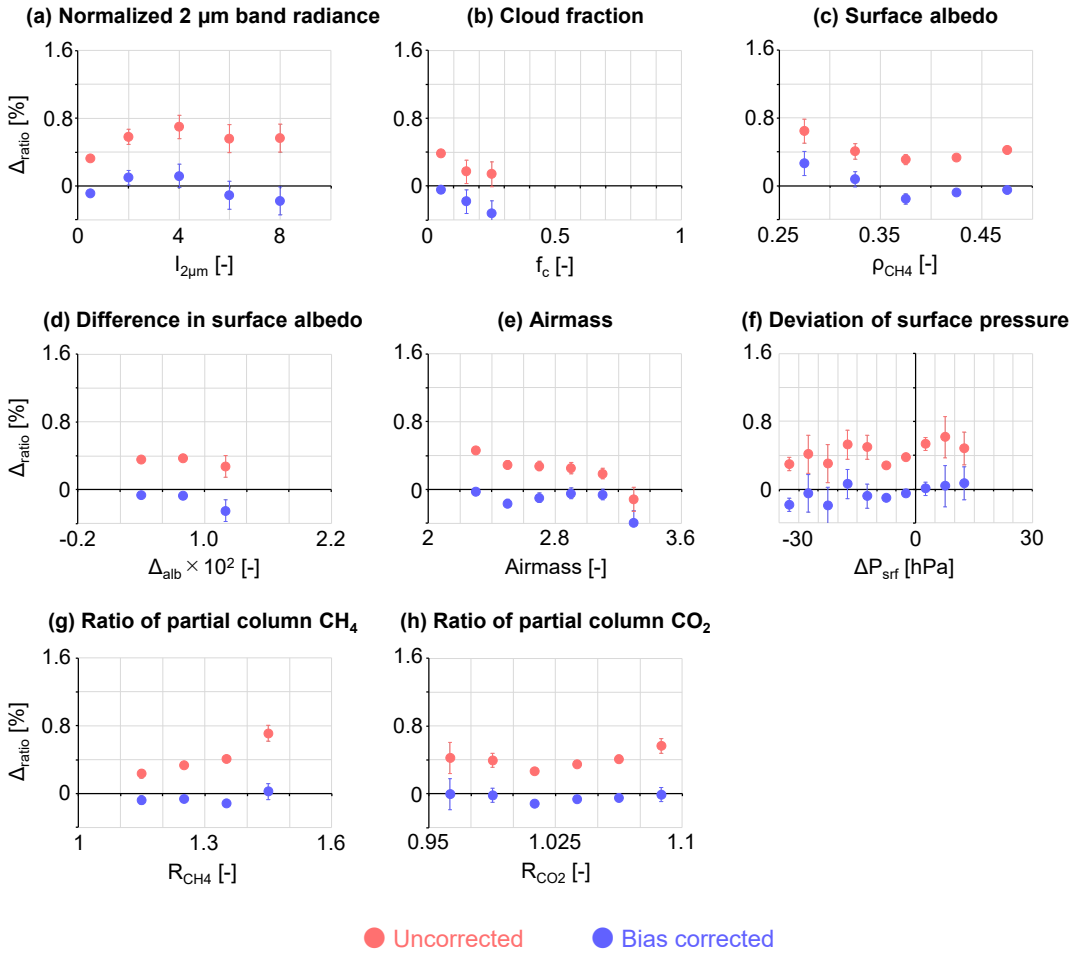

Figure A5. Relationship between the relative difference in the ratio component between GOSAT and TCCON (Δ_{ratio}) and the related variables for the GOSAT data acquired with gain M: (**a**) normalized 2 μm band radiance ($I_{2\mu m}$); (**b**) cloud fraction (f_c); (**c**) retrieved surface albedo of CH_4 band (ρ_{CH4}); (**d**) difference in the retrieved surface albedo (CH_4 band minus CO_2 band, Δ_{alb}); (**e**) airmass (A_m); (**f**) deviation of the retrieved clear-sky surface pressure from its prior (ΔP_{srf}); (**g**,**h**) ratio between the partial column-averaged dry-air mole fractions for the lower atmosphere and that for the upper atmosphere (R_{CH4} and R_{CO2}). Mean Δ_{ratio} for each bin is plotted for the bias-uncorrected and bias-corrected data.

References

1. Buchwitz, M.; de Beek, R.; Burrows, J.P.; Bovensmann, H.; Warneke, T.; Notholt, J.; Meirink, J.F.; Goede, A.P.H.; Bergamaschi, P.; Körner, S.; et al. Atmospheric methane and carbon dioxide from SCIAMACHY satellite data: Initial comparison with chemistry and transport models. *Atmos. Chem. Phys.* **2005**, *5*, 941–962. [CrossRef]
2. Frankenberg, C.; Meirink, J.F.; van Weele, M.; Platt, U.; Wagner, T. Assessing methane emissions from global space-borne observations. *Science* **2005**, *308*, 1010–1014. [CrossRef] [PubMed]
3. Parker, R.; Boesch, H.; Cogan, A.; Fraser, A.; Feng, L.; Palmer, P.I.; Messerschmidt, J.; Deutscher, N.; Griffith, D.W.T.; Notholt, J.; et al. Methane observations from the Greenhouse Gases Observing SATellite: Comparison to ground-based TCCON data and model calculations. *Geophys. Res. Lett.* **2011**, *38*, L15807. [CrossRef]
4. Butz, A.; Guerlet, S.; Hasekamp, O.; Schepers, D.; Galli, A.; Aben, I.; Frankenberg, C.; Hartmann, J.-M.; Tran, H.; Kuze, A.; et al. Toward accurate CO_2 and CH_4 observations from GOSAT. *Geophys. Res. Lett.* **2011**, *38*, L14812. [CrossRef]

5. Yoshida, Y.; Ota, Y.; Eguchi, N.; Kikuchi, N.; Nobuta, K.; Tran, H.; Morino, I.; Yokota, T. Retrieval algorithm for CO_2 and CH_4 column abundances from short-wavelength infrared spectral observations by the Greenhouse gases observing satellite. *Atmos. Meas. Tech.* **2011**, *4*, 717–734. [CrossRef]
6. Hu, H.; Landgraf, J.; Detmers, R.; Borsdorff, T.; de Brugh, J.A.; Aben, I.; Butz, A.; Hasekamp, O. Toward global mapping of methane with TROPOMI: First results and intersatellite comparison to GOSAT. *Geophys. Res. Lett.* **2018**, *45*, 3682–3689. [CrossRef]
7. Bergamaschi, P.; Frankenberg, C.; Meirink, J.F.; Krol, M.; Dentener, F.; Wagner, T.; Platt, U.; Kaplan, J.O.; Körner, S.; Heimann, M.; et al. Satellite chartography of atmospheric CH_4 from SCIAMACHY on board ENVISAT: 2. Evaluation based on inverse model simulations. *J. Geophys. Res.-Atmos.* **2007**, *112*, D02304. [CrossRef]
8. Monteil, G.; Houweling, S.; Butz, A.; Guerlet, S.; Schepers, D.; Hasekamp, O.; Frankenberg, C.; Scheepmaker, R.; Aben, I.; Röckmann, T. Comparison of CH_4 inversions based on 15 months of GOSAT and SCIAMACHY observations. *J. Geophys. Res.-Atmos.* **2013**, *118*, 11807–11823. [CrossRef]
9. Cressot, C.; Chevallier, F.; Bousquet, P.; Crevoisier, C.; Dlugokencky, E.J.; Fortems-Cheiney, A.; Frankenberg, C.; Parker, R.; Pison, I.; Scheepmaker, R.A.; et al. On the consistency between global and regional methane emissions inferred from SCIAMACHY, TANSO-FTS, IASI and surface measurements. *Atmos. Chem. Phys.* **2014**, *14*, 577–592. [CrossRef]
10. Alexe, M.; Bergamaschi, P.; Segers, A.; Detmers, R.; Butz, A.; Hasekamp, O.; Guerlet, S.; Parker, R.; Boesch, H.; Frankenberg, C.; et al. Inverse modelling of CH_4 emissions for 2010–2011 using different satellite retrieval products from GOSAT and SCIAMACHY. *Atmos. Chem. Phys.* **2015**, *15*, 113–133. [CrossRef]
11. Turner, A.J.; Jacob, D.J.; Wecht, K.J.; Maasakkers, J.D.; Lundgren, E.; Andrews, A.E.; Biraud, S.C.; Boesch, H.; Bowman, K.W.; Deutscher, N.M.; et al. Estimating global and North American methane emissions with high spatial resolution using GOSAT satellite data. *Atmos. Chem. Phys.* **2015**, *15*, 7049–7069. [CrossRef]
12. Meirink, J.F.; Eskes, H.J.; Goede, A.P.H. Sensitivity analysis of methane emissions derived from SCIAMACHY observations through inverse modelling. *Atmos. Chem. Phys.* **2006**, *6*, 1275–1292. [CrossRef]
13. GHG-CCI project team. User Requirements Document (URD) for the Essential Climate Variable (ECV) Greenhouse Gases (GHG), Version 2.1 (URDv2.1). 2016. Available online: http://cci.esa.int/sites/default/files/URDv2.1_GHG-CCI_Final.pdf (accessed on 15 May 2020).
14. O'Brien, D.M.; Rayner, P.J. Global observations of the carbon budget 2. CO_2 column from differential absorption of reflected sunlight in the 1.61 μm band of CO_2. *J. Geophys. Res.-Atmos.* **2002**, *107*, 4354.
15. Kuang, Z.; Margolis, J.; Toon, G.; Crisp, D.; Yung, Y. Spaceborne measurements of atmospheric CO_2 by high-resolution NIR spectrometry of reflected sunlight: An introductory study. *Geophys. Res. Lett.* **2002**, *29*, 1716. [CrossRef]
16. Dufour, E.; Bréon, F.-M. Spaceborne estimate of atmospheric CO_2 column by use of the differential absorption method: Error analysis. *Appl. Optics* **2003**, *42*, 3595–3609. [CrossRef]
17. Connor, B.J.; Boesch, H.; Toon, G.; Sen, B.; Miller, C.; Crisp, D. Orbiting Carbon Observatory: Inverse method and prospective error analysis. *J. Geophys. Res.-Atmos.* **2008**, *113*, D05305. [CrossRef]
18. Butz, A.; Hasekamp, O.P.; Frankenberg, C.; Aben, I. Retrievals of atmospheric CO_2 from simulated space-borne measurements of backscattered near-infrared sunlight: Accounting for aerosol effects. *Appl. Opt.* **2009**, *48*, 3322–3336. [CrossRef]
19. Schepers, D.; Guerlet, S.; Butz, A.; Landgraf, J.; Frankenberg, C.; Hasekamp, O.; Blavier, J.-F.; Deutscher, N.M.; Griffith, D.W.T.; Hase, F.; et al. Methane retrievals from Greenhouse Gases Observing Satellite (GOSAT) shortwave infrared measurements: Performance comparison of proxy and physics retrieval algorithms. *J. Geophys. Res.-Atmos.* **2012**, *117*, D10307. [CrossRef]
20. Cogan, A.J.; Boesch, H.; Parker, R.J.; Feng, L.; Palmer, P.I.; Blavier, J.-F.L.; Deutscher, N.M.; Macatangay, R.; Notholt, J.; Roehl, C.; et al. Atmospheric carbon dioxide retrieved from the Greenhouse gases Observing SATellite (GOSAT): Comparison with ground-based TCCON observations and GEOS-Chem model calculations. *J. Geophys. Res.-Atmos.* **2012**, *117*, D21301. [CrossRef]
21. Yoshida, Y.; Kikuchi, N.; Morino, I.; Uchino, O.; Oshchepkov, S.; Bril, A.; Saeki, T.; Schutgens, N.; Toon, G.C.; Wunch, D.; et al. Improvement of the retrieval algorithm for GOSAT SWIR XCO_2 and XCH_4 and their validation using TCCON data. *Atmos. Meas. Tech.* **2013**, *6*, 1533–1547. [CrossRef]

22. O'Dell, C.W.; Eldering, A.; Wennberg, P.O.; Crisp, D.; Gunson, M.R.; Fisher, B.; Frankenberg, C.; Kiel, M.; Lindqvist, H.; Mandrake, L.; et al. Improved retrievals of carbon dioxide from Orbiting Carbon Observatory-2 with the version 8 ACOS algorithm. *Atmos. Meas. Tech.* **2018**, *11*, 6539–6576. [CrossRef]
23. Butz, A.; Hasekamp, O.P.; Frankenberg, C.; Vidot, J.; Aben, I. CH_4 retrievals from space-based solar backscatter measurements: Performance evaluation against simulated aerosol and cirrus loaded scenes. *J. Geophys. Res.-Atmos.* **2010**, *115*, D24302. [CrossRef]
24. Parker, R.J.; Boesch, H.; Byckling, K.; Webb, A.J.; Palmer, P.I.; Feng, L.; Bergamaschi, P.; Chevallier, F.; Notholt, J.; Deutscher, N.; et al. Assessing 5 years of GOSAT Proxy XCH_4 data and associated uncertainties. *Atmos. Meas. Tech.* **2015**, *8*, 4785–4801. [CrossRef]
25. Fraser, A.; Palmer, P.I.; Feng, L.; Bösch, H.; Parker, R.; Dlugokencky, E.J.; Krummel, P.B.; Langenfelds, R.L. Estimating regional fluxes of CO_2 and CH_4 using space-borne observations of XCH_4: XCO_2. *Atmos. Chem. Phys.* **2014**, *14*, 12883–12895. [CrossRef]
26. Pandey, S.; Houweling, S.; Krol, M.; Aben, I.; Chevallier, F.; Dlugokencky, E.J.; Gatti, L.V.; Gloor, E.; Miller, J.B.; Detmers, R.; et al. Inverse modeling of GOSAT-retrieved ratios of total column CH_4 and CO_2 for 2009 and 2010. *Atmos. Chem. Phys.* **2016**, *16*, 5043–5062. [CrossRef]
27. Feng, L.; Palmer, P.I.; Bösch, H.; Parker, R.J.; Webb, A.J.; Correia, C.S.C.; Deutscher, N.M.; Domingues, L.G.; Feist, D.G.; Gatti, L.V.; et al. Consistent regional fluxes of CH_4 and CO_2 inferred from GOSAT proxy XCH_4: XCO_2 retrievals, 2010–2014. *Atmos. Chem. Phys.* **2017**, *17*, 4781–4797. [CrossRef]
28. GHG-CCI project team. Algorithm inter-comparison and error characterization & analysis report (AIECAR) of the GHG-CCI project of ESA's Climate Change Initiative, Version 1 (AIECARv1). 2012. Available online: http://www.iup.uni-bremen.de/~{}buch/ghgcci_public/AIECARv1_GHG-CCI_Final.pdf (accessed on 15 May 2020).
29. Parker, R.J.; Webb, A.; Boesch, H.; Somkuti, P.; Barrio Guillo, R.; Di Noia, A.; Kalaitzi, N.; Anand, J.; Bergamaschi, P.; Chevallier, F.; et al. A Decade of GOSAT Proxy Satellite CH_4 Observations. *Earth Syst. Sci. Data Discuss.* **2020**, in review.
30. Detmers, R.; Hasekamp, O. Product User Guide (PUG) for the RemoTeC XCH_4 PROXY GOSAT Data Product v2.3.8. 2016. Available online: ftp://ftp.sron.nl/pub/pub/RemoTeC/TEMIS/CRDP4/DOCS/PUGv4p1_CH4_GOS_SRPR.pdf (accessed on 8 March 2020).
31. GHG-CCI project team. Product User Guide (PUGv4) for the University of Leicester Proxy XCH_4 GOSAT Data Product (CH4_GOS_OCPR). 2016. Available online: https://catalogue.ceda.ac.uk/uuid/4774bc5719754c44add5c6f209fc25ae (accessed on 8 March 2020).
32. Yoshida, Y.; Kikuchi, N.; Yokota, T. On-orbit radiometric calibration of SWIR bands of TANSO-FTS onboard GOSAT. *Atmos. Meas. Tech.* **2012**, *5*, 2515–2523. [CrossRef]
33. Ishida, H.; Nakajima, T.Y. Development of an unbiased cloud detection algorithm for a spaceborne multispectral imager. *J. Geophys. Res.-Atmos.* **2009**, *114*, D07206. [CrossRef]
34. Yoshida, Y.; Eguchi, N.; Ota, Y.; Kikuchi, N.; Nobuta, K.; Aoki, T.; Yokota, T. Algorithm theoretical basis document (ATBD) for CO_2, CH_4 and H_2O column amounts retrieval from GOSAT TANSO-FTS SWIR. 2017. Available online: http://data2.gosat.nies.go.jp/doc/documents/ATBD_FTSSWIRL2_V2.0_en.pdf (accessed on 8 March 2020).
35. Nakajima, T.; Nakajima, T.Y.; Higurashi, A.; Sano, I.; Takamura, T.; Ishida, H.; Schutgens, N. A study of aerosol and cloud information retrievals from CAI imager on board GOSAT satellite. *J. Remote Sens. Soc. Japan.* **2008**, *28*, 178–189, (in Japanese with English abstract and figure captions).
36. Guerlet, S.; Butz, A.; Schepers, D.; Basu, S.; Hasekamp, O.P.; Kuze, A.; Yokota, T.; Blavier, J.-F.; Deutscher, N.M.; Griffith, D.W.T. Impact of aerosol and thin cirrus on retrieving and validating XCO_2 from GOSAT shortwave infrared measurements. *J. Geophys. Res.-Atmos.* **2013**, *118*, 4887–4905. [CrossRef]
37. Inoue, M.; Morino, I.; Uchino, O.; Nakatsuru, T.; Yoshida, Y.; Yokota, T.; Wunch, D.; Wennberg, P.O.; Roehl, C.M.; Griffith, D.W.T.; et al. Bias corrections of GOSAT SWIR XCO_2 and XCH_4 with TCCON data and their evaluation using aircraft measurement data. *Atmos. Meas. Tech.* **2016**, *9*, 3491–3512. [CrossRef]
38. Christi, M.J.; Stephens, G.L. Retrieving profiles of atmospheric CO_2 in clear sky and in the presence of thin cloud using spectroscopy from the near and thermal infrared: A preliminary case study. *J. Geophys. Res.-Atmos.* **2004**, *109*, D04316. [CrossRef]

39. Wunch, D.; Wennberg, P.O.; Toon, G.C.; Connor, B.J.; Fisher, B.; Osterman, G.B.; Frankenberg, C.; Mandrake, L.; O'Dell, C.; Ahonen, P.; et al. A method for evaluating bias in global measurements of CO_2 total columns from space. *Atmos. Chem. Phys.* **2011**, *11*, 12317–12337. [CrossRef]
40. Taylor, T.E.; O'Dell, C.W.; O'Brien, D.M.; Kikuchi, N.; Yokota, T.; Nakajima, T.Y.; Ishida, H.; Crisp, D.; Nakajima, T. Comparison of cloud-screening methods applied to GOSAT near-infrared spectra. *IEEE Trans. Geosci. Remote Sens.* **2012**, *50*, 295–309. [CrossRef]
41. Notholt, J.; Schrems, O.; Warneke, T.; Deutscher, N.; Weinzierl, C.; Palm, M.; Buschmann, M.; AWI-PEV Station Engineers. TCCON data from Ny Alesund, Spitzbergen, Norway, Release GGG2014R1, TCCON Data Archive. Available online: https://data.caltech.edu/records/1289 (accessed on 8 March 2020).
42. Kivi, R.; Heikkinen, P.; Kyro, E. TCCON data from Sodankyla, Finland, Release GGG2014R0, TCCON Data Archive. Available online: https://data.caltech.edu/records/289 (accessed on 8 March 2020).
43. Wunch, D.; Mendonca, J.; Colebatch, O.; Allen, N.; Blavier, J.-F.L.; Springett, S.; Worthy, D.; Kessler, R.; Strong, K. TCCON data from East Trout Lake, Canada, Release GGG2014R1, TCCON Data Archive. Available online: https://data.caltech.edu/records/362 (accessed on 8 March 2020).
44. Deutscher, N.; Notholt, J.; Messerschmidt, J.; Weinzierl, C.; Warneke, T.; Petri, C.; Grupe, P. TCCON data from Bialystok, Poland, Release GGG2014R2, TCCON Data Archive. Available online: https://data.caltech.edu/records/267 (accessed on 8 March 2020).
45. Notholt, J.; Petri, C.; Warneke, T.; Deutscher, N.; Buschmann, M.; Weinzierl, C.; Macatangay, R.; Grupe, P. TCCON data from Bremen, Germany, Release GGG2014R1, TCCON Data Archive. Available online: https://data.caltech.edu/records/268 (accessed on 8 March 2020).
46. Hase, F.; Blumenstock, T.; Dohe, S.; Groß, J.; Kiel, M. TCCON data from Karlsruhe, Germany, Release GGG2014R1, TCCON Data Archive. Available online: https://data.caltech.edu/records/278 (accessed on 8 March 2020).
47. Té, Y.; Jeseck, P.; Janssen, C. TCCON data from Paris (FR), Release GGG2014.R0, TCCON Data Archive. Available online: https://data.caltech.edu/records/284 (accessed on 8 March 2020).
48. Warneke, T.; Messerschmidt, J.; Notholt, J.; Weinzierl, C.; Deutscher, N.; Petri, C.; Grupe, P.; Vuillemin, C.; Truong, F.; Schmidt, M.; et al. TCCON data from Orleans, France, Release GGG2014R1, TCCON Data Archive. Available online: https://data.caltech.edu/records/283 (accessed on 8 March 2020).
49. Sussmann, R.; Rettinger, M. TCCON data from Garmisch, Germany, Release GGG2014R2, TCCON Data Archive. Available online: https://data.caltech.edu/records/956 (accessed on 8 March 2020).
50. Wennberg, P.O.; Roehl, C.; Wunch, D.; Toon, G.C.; Blavier, J.-F.; Washenfelder, R.; Keppel-Aleks, G.; Allen, N.; Ayers, J. TCCON data from Park Falls, Wisconsin, USA, Release GGG2014R1, TCCON Data Archive. Available online: https://data.caltech.edu/records/295 (accessed on 8 March 2020).
51. Morino, I.; Yokozeki, N.; Matzuzaki, T.; Horikawa, M. TCCON Data from Rikubetsu, Hokkaido, Japan, Release GGG2014R2, TCCON Data Archive. Available online: https://data.caltech.edu/records/957 (accessed on 8 March 2020).
52. Iraci, L.; Podolske, J.; Hillyard, P.; Roehl, C.; Wennberg, P.O.; Blavier, J.-F.; Landeros, J.; Allen, N.; Wunch, D.; Zavaleta, J.; et al. TCCON data from Indianapolis, Indiana, USA, Release GGG2014R1, TCCON Data Archive. Available online: https://data.caltech.edu/records/274 (accessed on 8 March 2020).
53. Dubey, M.; Lindenmaier, R.; Henderson, B.; Green, D.; Allen, N.; Roehl, C.; Blavier, J.-F.; Butterfield, Z.; Love, S.; Hamelmann, J.; et al. TCCON data from Four Corners, NM, USA, Release GGG2014R0, TCCON data archive, TCCON Data Archive. Available online: https://data.caltech.edu/records/272 (accessed on 8 March 2020).
54. Wennberg, P.O.; Wunch, D.; Roehl, C.; Blavier, J.-F.; Toon, G.C.; Allen, N.; Dowell, P.; Teske, K.; Martin, C.; Martin, J. TCCON data from Lamont, Oklahoma, USA, Release GGG2014R1, TCCON Data Archive. Available online: https://data.caltech.edu/records/279 (accessed on 8 March 2020).
55. Goo, T.-Y.; Oh, Y.-S.; Velazco, V.A. TCCON data from Anmeyondo, South Korea, Release GGG2014R0, TCCON Data Archive. Available online: https://data.caltech.edu/records/266 (accessed on 8 March 2020).
56. Morino, I.; Matsuzaki, T.; Horikawa, M. TCCON data from Tsukuba, Ibaraki, Japan, 125HR, Release GGG2014R2, TCCON Data Archive. Available online: https://data.caltech.edu/records/958 (accessed on 8 March 2020).

57. Iraci, L.; Podolske, J.; Hillyard, P.; Roehl, C.; Wennberg, P.O.; Blavier, J.-F.; Landeros, J.; Allen, N.; Wunch, D.; Zavaleta, J.; et al. TCCON data from Armstrong Flight Research Center, Edwards, CA, USA, Release GGG2014R1, TCCON Data Archive. Available online: https://data.caltech.edu/records/270 (accessed on 8 March 2020).
58. Wennberg, P.O.; Roehl, C.; Blavier, J.-F.; Wunch, D.; Landeros, J.; Allen, N. TCCON data from Jet Propulsion Laboratory, Pasadena, California, USA, Release GGG2014R1, TCCON Data Archive. Available online: https://data.caltech.edu/records/277 (accessed on 8 March 2020).
59. Wennberg, P.O.; Wunch, D.; Roehl, C.; Blavier, J.-F.; Toon, G.C.; Allen, N. TCCON data from California Institute of Technology, Pasadena, California, USA, Release GGG2014R1, TCCON Data Archive. Available online: https://data.caltech.edu/records/285 (accessed on 8 March 2020).
60. Kawakami, S.; Ohyama, H.; Arai, K.; Okumura, H.; Taura, C.; Fukamachi, T.; Sakashita, M. TCCON data from Saga, Japan, Release GGG2014R0, TCCON Data Archive. Available online: https://data.caltech.edu/records/288 (accessed on 8 March 2020).
61. Liu, C.; Wang, W.; Sun, Y. TCCON data from Hefei, China, Release GGG2014R0, TCCON Data Archive. Available online: https://data.caltech.edu/records/1092 (accessed on 8 March 2020).
62. Morino, I.; Velazco, V.A.; Hori, A.; Uchino, O.; Griffith, D.W.T. TCCON data from Burgos, Philippines, Release GGG2014R0, TCCON Data Archive. Available online: https://data.caltech.edu/records/1090 (accessed on 8 March 2020).
63. Dubey, M.; Henderson, B.; Green, D.; Butterfield, Z.; Keppel-Aleks, G.; Allen, N.; Blavier, J.-F.; Roehl, C.; Wunch, D.; Lindenmaier, R. TCCON data from Manaus, Brazil, Release GGG2014R0, TCCON Data Archive. Available online: https://data.caltech.edu/records/282 (accessed on 8 March 2020).
64. Griffith, D.W.T.; Deutscher, N.; Velazco, V.A.; Wennberg, P.O.; Yavin, Y.; Keppel Aleks, G.; Washenfelder, R.; Toon, G.C.; Blavier, J.-F.; Paton, W.C.; et al. TCCON data from Darwin, Australia, Release GGG2014R0, TCCON Data Archive. Available online: https://data.caltech.edu/records/269 (accessed on 8 March 2020).
65. Griffith, D.W.T.; Velazco, V.A.; Deutscher, N.; Paton, W.C.; Jones, N.; Wilson, S.; Macatangay, R.; Kettlewell, G.; Buchholz, R.R.; Riggenbach, M. TCCON data from Wollongong, Australia, Release GGG2014R0, TCCON Data Archive. 2017. Available online: https://data.caltech.edu/records/291 (accessed on 8 March 2020).
66. Sherlock, V.; Connor, B.; Robinson, J.; Shiona, H.; Smale, D.; Pollard, D. TCCON data from Lauder, New Zealand, 120HR, Release GGG2014R0, TCCON Data Archive. Available online: https://data.caltech.edu/records/280 (accessed on 8 March 2020).
67. Sherlock, V.; Connor, B.; Robinson, J.; Shiona, H.; Smale, D.; Pollard, D. TCCON data from Lauder, New Zealand, 125HR, Release GGG2014R0, TCCON Data Archive. Available online: https://data.caltech.edu/records/281 (accessed on 8 March 2020).
68. Dils, B.; Buchwitz, M.; Reuter, M.; Schneising, O.; Boesch, H.; Parker, R.; Guerlet, S.; Aben, I.; Blumenstock, T.; Burrows, J.P.; et al. The Greenhouse Gas Climate Change Initiative (GHG-CCI): Comparative validation of GHG-CCI SCIAMACHY/ENVISAT and TANSO-FTS/GOSAT CO_2 and CH_4 retrieval algorithm products with measurements from the TCCON. *Atmos. Meas. Tech.* **2014**, *7*, 1723–1744. [CrossRef]
69. Wunch, D.; Toon, G.C.; Blavier, J.-F.L.; Washenfelder, R.A.; Notholt, J.; Connor, B.J.; Griffith, D.W.T.; Sherlock, V.; Wennberg, P.O. The Total Carbon Column Observing Network. *Phil. Trans. R. Soc. A* **2011**, *369*, 2087–2112. [CrossRef]
70. Deutscher, N.M.; Griffith, D.W.T.; Bryant, G.W.; Wennberg, P.O.; Toon, G.C.; Washenfelder, R.A.; Keppel-Aleks, G.; Wunch, D.; Yavin, Y.; Allen, N.T.; et al. Total column CO_2 measurements at Darwin, Australia—Site description and calibration against in situ aircraft profiles. *Atmos. Meas. Tech.* **2010**, *3*, 947–958. [CrossRef]
71. Mendonca, J.; Strong, K.; Wunch, D.; Toon, G.C.; Long, D.A.; Hodges, J.T.; Sironneau, V.T.; Franklin, J.E. Using a speed-dependent Voigt line shape to retrieve O_2 from Total Carbon Column Observing Network solar spectra to improve measurements of XCO_2. *Atmos. Meas. Tech.* **2019**, *12*, 35–50. [CrossRef]
72. Schneising, O.; Heymann, J.; Buchwitz, M.; Reuter, M.; Bovensmann, H.; Burrows, J.P. Anthropogenic carbon dioxide source areas observed from space: Assessment of regional enhancements and trends. *Atmos. Chem. Phys.* **2013**, *13*, 2445–2454. [CrossRef]
73. Kivi, R.; Heikkinen, P. Fourier transform spectrometer measurements of column CO_2 at Sodankylä, Finland. *Geosci. Instrum. Method. Data Syst.* **2016**, *5*, 271–279. [CrossRef]

74. Lindenmaier, R.; Dubey, M.K.; Henderson, B.G.; Butterfield, Z.T.; Herman, J.R.; Rahn, T.; Lee, S.-H. Multiscale observations of CO_2, $^{13}CO_2$, and pollutants at Four Corners for emission verification and attribution. *Proc. Natl. Acad. Sci. USA* **2014**, *111*, 8386–8391. [CrossRef] [PubMed]
75. Kort, E.A.; Frankenberg, C.; Costigan, K.R.; Lindenmaier, R.; Dubey, M.K.; Wunch, D. Four corners: The largest US methane anomaly viewed from space. *Geophys. Res. Lett.* **2014**, *41*, 6898–6903. [CrossRef]
76. Kuze, A.; Suto, H.; Shiomi, K.; Urabe, T.; Nakajima, M.; Yoshida, J.; Kawashima, T.; Yamamoto, Y.; Kataoka, F.; Buijs, H. Level 1 algorithms for TANSO on GOSAT: Processing and on-orbit calibrations. *Atmos. Meas. Tech.* **2012**, *5*, 2447–2467. [CrossRef]

© 2020 by the authors. Licensee MDPI, Basel, Switzerland. This article is an open access article distributed under the terms and conditions of the Creative Commons Attribution (CC BY) license (http://creativecommons.org/licenses/by/4.0/).